

# Constraining On- and Off-Fault Nonlinear Dynamic Rupture Parameters via Hierarchical Bayesian Inversion for the 2019 Mw 7.1 Ridgecrest Earthquake

Zihua Niu<sup>a</sup>, Maximilian Kruse<sup>b</sup>, Linus Seelinger<sup>b</sup>, Nico Schliwa<sup>a</sup>, Heiner Igel<sup>a</sup> and Alice-Agnes Gabriel<sup>c,a,\*</sup>

<sup>a</sup>Department of Earth and Environmental Sciences, Ludwig-Maximilians-Universität München, Munich, Germany, Munich, Germany

<sup>b</sup>Scientific Computing Center, Karlsruhe Institute of Technology, Karlsruhe, Germany

<sup>c</sup>Department of Informatics, Technical University of Munich, Munich, Germany, Munich, Germany

<sup>d</sup>Scripps Institution of Oceanography, UC San Diego, La Jolla, CA, USA

## ARTICLE INFO

### Keywords:

Bayesian inversion  
High-performance computing  
Earthquake source inversion  
Dynamic rupture simulation

## ABSTRACT


We present the first multilevel Bayesian inversion to quantify uncertainties and correlations among on- and off-fault dynamic rupture parameters for the 2019  $M_w$  7.1 Ridgecrest earthquake. The inversion is constrained by multidisciplinary surface deformation data, including fault-parallel offsets from satellite imagery, high-rate GNSS time series, and static GNSS displacements, and is enabled by more than four million CPU hours of 3D dynamic rupture simulations. Our realistic rupture models incorporate strong velocity-weakening rate-and-state friction and off-fault plasticity. We find a strong correlation between on-fault frictional weakening and off-fault plasticity: increased inelastic deformation can compensate for more prominent velocity-weakening friction in the northwestern part of the fault. The preferred dynamic rupture models reduce velocity weakening from northwest to southeast along the main fault. This improves the fit with observed fault-parallel surface offsets, consistent with along-strike variations in fault maturity. The inversion favors low off-fault plastic cohesion, which improves the fit to observed surface offsets and is consistent with shallow damage zones imaged geophysically. We infer a shallow slip deficit (SSD) of 13.1% with a standard deviation of 5.1%. Notably, 55% of the models fall within the 8–32% SSD range estimated from previous kinematic inversions, implying that co-seismic off-fault inelasticity is crucial to explain the observed SSD. Our results demonstrate the feasibility of integrating 3D dynamic rupture simulations with multilevel Bayesian inversion to constrain nonlinear dynamic rupture processes and off-fault properties, toward probabilistic, physics-based earthquake source characterization and uncertainty quantification grounded in observational constraints.

## 1. Introduction

The  $M_w$  7.1 Ridgecrest earthquake struck California on 5 July 2019 (Ross et al., 2019) and ruptured across a complicated multi-fault system (e.g., DuRoss et al., 2020). Multiple types of observations captured the event, including strong ground motion seismic records (Hauksson et al., 2020), global navigation satellite system (GNSS) co-seismic displacements (Melgar et al., 2020; Floyd et al., 2020), and fault displacement discontinuities (Antoine et al., 2021), hereafter referred to as “offsets”, from optical image correlation using satellite images. These high-quality datasets have enhanced data-driven interpretation of the Ridgecrest earthquake, particularly through kinematic finite-fault inversions (e.g., Goldberg et al., 2020), although the resulting models show large variability (Wang et al., 2020).

Dynamic rupture simulations (Harris et al., 2018) can incorporate physical laws and complex subsurface structures to better constrain earthquake processes. Taufiqurrahman et al. (2023) developed a 3D dynamic rupture model of the  $M_w$  7.1 Ridgecrest earthquake that integrates long- and short-term stress changes, seismic and geodetic data, a 3D velocity model, conjugate fault geometries, topography, and off-fault visco-plasto-elastic deformation (Text S1). Yet, how reliably surface displacement data can constrain on-fault frictional parameters and off-fault inelastic deformation, and the extent of their trade-offs, remains statistically unresolved. In particular, while fault friction parameters are

\*Corresponding author

 aangniu96@gmail.com (Z. Niu); maximilian.kruse@kit.edu (M. Kruse); mail@linusseelinger.de (L. Seelinger); nico.schliwa@gmx.de (N. Schliwa); heiner.igel@lmu.de (H. Igel); algabriel@ucsd.edu (A. Gabriel)  
ORCID(s): 0009-0004-7825-9458 (N. Schliwa); 0000-0003-0112-8412 (A. Gabriel)

partly constrained by laboratory studies (e.g., Marone, 1998), direct observational constraints on off-fault inelastic properties remain difficult to constrain due to the scarcity of high-resolution, near-fault field observations (e.g., Roten et al., 2014).

Off-fault inelasticity is a key mechanism affecting earthquake physics. Accurately resolving off-fault plasticity and damage properties is essential for modeling near-fault ground motions (e.g., Andrews, 2005; Niu et al., 2025b) and (multi-fault) rupture dynamics (e.g., Finzi and Langer, 2012; Gabriel et al., 2013; Niu et al., 2025a). Off-fault deformation may also help explain the commonly observed deficit in near-surface fault slip, known as ‘shallow slip deficit’ (SSD, Fialko et al., 2005). For the 2019 Ridgecrest mainshock, SSD estimates reach up to 45% (Wang et al., 2020). Multiple mechanisms have been proposed to explain (apparent) SSDs, including post-/interseismic creep, modeling artifacts, and sparse data coverage (e.g., Marchandon et al., 2021). For most earthquakes, including the 2019 Ridgecrest earthquake, these effects may not be large enough to account for the observed SSD (e.g., Antoine et al., 2024). Therefore, co-seismic inelastic off-fault deformation has been proposed as a dominant contributor (e.g., Kaneko et al., 2010; Roten et al., 2017a).

Despite the growing availability of high-quality surface observations, uncertainty quantification using physics-based dynamic rupture simulations remains challenging. One challenge lies in the computational expense, as 3D dynamic rupture simulations of real earthquakes typically require thousands to hundreds of thousands of CPU hours per model realization (e.g., Uphoff et al., 2017; Roten et al., 2014; Gabriel et al., 2023). Dynamic rupture earthquake inversions date back to Mikumo et al. (1987), who used a simplified rupture criterion based on a locking fracture model. Subsequent studies, such as Peyrat and Olsen (2004) and Twardzik et al. (2014), used fully spontaneous dynamic rupture simulations and the neighborhood algorithm (Sambridge, 1999), a nonlinear derivative-free technique, to estimate best-fit models without quantifying uncertainties. For dynamic source inversion with uncertainty analysis (Gallovič et al., 2019), Bayesian inversion based on Markov chain Monte Carlo sampling (MCMC, Hastings, 1970) requires minimal assumptions, however, typically requires thousands to millions of forward simulations (Premus et al., 2022; Schliwa et al., 2024).

Here, we present the first Bayesian inversion of geometrically complex 3D dynamic rupture simulations with off-fault plasticity that jointly resolves on- and off-fault nonlinear parameters, using high-resolution satellite imagery and GNSS data. Rather than reducing the computational cost of individual forward simulations, we reduce the number of costly simulations required for uncertainty quantification employing the multilevel delayed acceptance (MLDA) algorithm (Lykkegaard et al., 2023). MLDA efficiently explores the parameter space by combining a hierarchy of fast approximate models with hundreds to thousands of fully resolved runs, correcting for approximation errors. Kruse et al. (2025) recently demonstrated the scalability and efficiency of this approach for large-scale geophysical models in an HPC environment, showing that asynchronous prefetching and surrogate models can provide near-optimal resource allocation in strong-scaling regimes. By leveraging MLDA within the UM-Bridge HPC modeling framework (Seelinger et al., 2023), we efficiently sample posterior distributions using fully resolved SeisSol (Gabriel et al., 2025) dynamic rupture simulations that include nonlinear rheology and realistic 3D subsurface structure. We apply this framework to the 2019  $M_w$  7.1 Ridgecrest earthquake, performing a Bayesian inversion for rate-and-state fault friction and Drucker–Prager off-fault plasticity parameters. The inversion is constrained by high-rate GNSS time series (Melgar et al., 2020), static GNSS displacements (Floyd et al., 2020), and fault-parallel offsets from satellite image correlation (Antoine et al., 2021). Our results reveal previously unresolved correlations between on-fault friction and off-fault inelastic deformation. We provide the first statistically constrained estimates of fault slip uncertainty and trade-offs with off-fault plasticity from physics-based dynamic rupture inversion. We quantitatively demonstrate that the SSD of the  $M_w$  7.1 Ridgecrest earthquake may be explained by co-seismic off-fault inelasticity. We highlight the potential of probabilistic and physics-based earthquake modeling that integrates observational data with nonlinear rupture dynamics.

## 2. Data and Methods

The objective of this study is to infer nonlinear on-fault and off-fault parameters governing 3D dynamic rupture, constrained by near-fault geodetic observations, and to quantify the associated uncertainties and parameter correlations. While our focus is the well-recorded 2019 Ridgecrest mainshock, our framework is broadly applicable to other earthquakes where high-resolution GNSS and satellite-derived surface deformation data are increasingly available. In this section, we first describe the geodetic datasets that we use to constrain the Bayesian dynamic rupture inversion. We then outline our application of a recently developed, parallelized implementation of the Multilevel Delayed Acceptance

(MLDA) algorithm (Kruse et al., 2025), which enables efficient Bayesian inference using computationally intensive dynamic rupture simulations.

## 2.1. Data

We use fault-parallel offsets from satellite images, high-rate displacement time series from 10 GNSS stations, and static displacements from 11 GNSS stations to constrain the inversion of nonlinear physical parameters in the dynamic rupture source inversion of the 2019 Ridgecrest mainshock. Fault-parallel surface offsets derived from optical image correlation along the modeled fault traces provide key constraints on shallow fault slip distribution. WorldView and Pleiades satellite images offer a ground resolution of 0.5 m and subpixel image correlation achieving displacement resolution down to 0.05 m (Antoine et al., 2021). We define  $\Delta u^{obs}(s)$  as the along-strike variation in fault-parallel offset, where  $s$  is the distance measured along-strike from the mainshock epicenter (dashed black line in Fig. 1).

We complement fault-parallel offsets with near-field surface displacement time series from high-rate GNSS stations, to better constrain rupture kinematics. The processed 1 Hz displacement time series from Melgar et al. (2020) have an accuracy of 0.05 m in each displacement component. For later reference, we denote the observed GNSS time series as  $u_i^{GT,obs}(t)$ , where the index  $i$  combines a direction component index  $j$  (north-south NS, east-west EW, or up-down UD) and a station index  $k$ . Additionally, we incorporate processed co-seismic static displacements from 11 additional GNSS stations provided by UNAVCO, with measurement accuracy between 1.5 and 2.1 mm (Floyd et al., 2020). We denote these observed co-seismic static displacements as  $u_i^{GS,obs}$ , where the index  $i$  again combines the direction component  $j$  and the station index  $k$ . We independently validate the inversion results against seismic recordings from near-fault strong-motion stations (blue triangles in Fig. 1a; see Section 3.2).

## 2.2. Dynamic rupture model parameters

3D earthquake dynamic rupture models combine nonlinear frictional failure along embedded 2D fault surfaces with seismic wave propagation through a 3D elastic or inelastic bulk rock model domain (Harris et al., 2018). The high-resolution reference dynamic rupture model of Taufiqurrahman et al. (2023) provides an important baseline for our inversion. We briefly summarize the rupture dynamics of the reference model in Text S1 and Fig. S1. We intend to infer four model parameters  $\mathbf{m} = (\alpha_0, \alpha_1, \gamma_0, \gamma_1)^T$  in this study (Table 1), parameterizing on- and off-fault dynamic rupture parameters.

### 2.2.1. Model resolution and reference rupture dynamics

For computational reasons, our MLDA algorithm uses two meshes both with a lower resolution compared to the reference model (Section 2.4). The two MLDA models utilize the same mesh, which has  $\sim 15\%$  of the mesh size of the high-resolution reference model (Text S2). This smaller mesh restricts the resolution of the seismic wavefield to 1.0 Hz close to the fault (instead of 2.0 Hz in the reference model), which is still sufficient to compare with the high-rate GNSS time series used in the inversion. We highlight that minor differences in rupture dynamics due to the coarser mesh do not adversely affect our inversion.

On-fault rupture dynamics are sensitive to on-fault mesh resolution (Day et al., 2005), and the process zone, the area behind the rupture front where shear stress drops from its static value to its dynamic value, must be resolved. In the reference model, the process zone size is  $>515$  m in 95% of all fault elements, and the reference model used 75 m on-fault resolution and polynomial basis functions of order 4. In our model setup, we use a fault element size of 200 m and basis functions of polynomial degree 3 to reduce computational cost. We observe differences in on-fault slip and peak slip rate at the bottom of the seismogenic zone between our high-resolution model and the reference solution (Fig. S4c,d), which are likely due to the complex rupture dynamics leading to deep rupture. In the reference model, a reflected surface rupture front dynamically triggers the deep part of the fault (Schliwa et al., 2025). Increasing resolution is unfortunately out of the scope of current computational capabilities (see Sec. 2.5). The observed differences in deep rupture dynamics and the resulting small differences in geodetic synthetics fall within the range of uncertainties in our Bayesian likelihood function in Eq. (8), as detailed in Table S1. We discuss differences in rupture dynamics between the high-resolution reference model and our two lower-resolution models in Text S3.

### 2.2.2. On-fault friction

During the inversion, we vary the parameterization of the strong velocity-weakening rate-and-state (SVW-RS) friction law (Dunham et al., 2011), which captures the pronounced reduction in co-seismic friction observed in

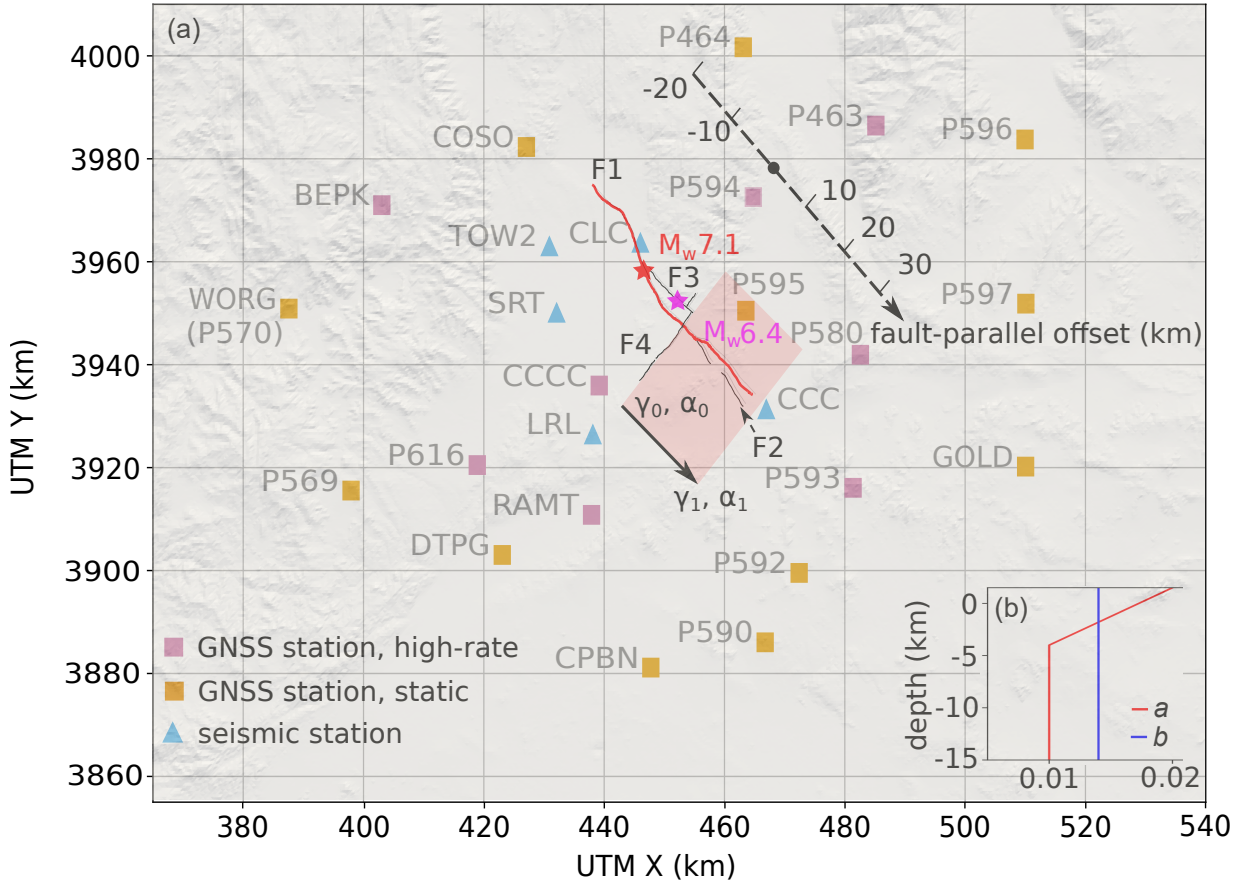


**Figure 1:** Data and model setup for the 3D dynamic rupture inversion. (a) Map view of the GNSS and seismic stations used to constrain the inversion, located within 100 km of the  $M_w$  7.1 Ridgecrest mainshock epicenter (red star). The fault trace (F1) of the main fault segment that ruptured during the 2019  $M_w$  7.1 Ridgecrest mainshock is shown as a solid red line, thinner black lines mark the secondary segment ruptured during the mainshock (F2), the subparallel fault (F3) where the  $M_w$  6.4 foreshock nucleated (pink star), and the conjugate fault (F4) that hosted the foreshock and re-ruptured during the mainshock, following (Taufiqurrahman et al., 2023). The 3D fault structure is shown in Fig. S2. Pink squares indicate GNSS stations with high-rate displacement time series from Melgar et al. (2020), and orange squares mark GNSS stations used for static co-seismic displacements from Floyd et al. (2020). Blue triangles denote locations of strong-motion seismic stations used to validate the inversion. The region of assumed along-strike spatial variation in plastic cohesion  $c$  and direct-effect parameter  $a$  is highlighted in red. The parameters  $c$  and  $a$  vary linearly in space from  $\gamma_0$  and  $\alpha_0$  to  $\gamma_1$  and  $\alpha_1$ , following the direction of the black arrow. Fault-parallel offset distances are measured along the dashed black axis. (b, Inset) Depth profiles of the reference direct-effect parameter  $a$  and the constant evolution-effect parameter  $b$ , as used in the strong velocity-weakening friction law (Eq. (6) in SI).

laboratory experiments at high slip rates (Di Toro et al., 2006). The mathematical formulation of the used SVW-RS friction law is given in Text S4 and all model parameters are listed in Table 1.

Among the SVW-RS friction parameters, we focus on the physically important parameter combination  $(a - b)$ , which governs the spontaneity and stability of dynamic rupture (Dunham et al., 2011). Limiting the inversion to a single friction parameter mitigates the high computational cost of each large-scale 3D dynamic rupture simulation, while ensuring accurate posterior probability estimates. The value of  $(a - b)$  determines how friction evolves with slip rate, where  $a - b < 0$  corresponds to velocity-weakening (VW) and  $a - b > 0$  to velocity-strengthening (VS) behavior. Earthquakes nucleate in VW regions, but fault friction may transition to a VS regime close to the Earth's surface, e.g., due to unconsolidated fault gouge (Kaneko and Fialko, 2011; Cakir et al., 2023). The depth profile of  $(a - b)$  plays a critical role in modeling shallow slip behavior during coseismic, postseismic, and interseismic periods (e.g., Barbot et al., 2012).



**Table 1**

Dynamic rupture model parameters, with  $\alpha_0$  and  $\alpha_1$  being scaling factors of the direct-effect parameter  $a$  in Eq. (1),  $L$  the characteristic slip distance,  $\gamma_0$  and  $\gamma_1$  are scaling factors for plastic cohesion  $c$  in Eq. (3), and  $\phi$  the bulk friction angle. The on-fault friction parameters that do not vary during the inversion are  $V_0$ ,  $f_0$ ,  $V_w$ ,  $f_w$ ,  $V_{init}$  and  $b$  in Eqs. (2) to (7) of the SI.

	Param.	Value	Units	Param.	Value	Units
off-fault	$\gamma_0$	[0.1, 2.0]	1	$\gamma_1$	[0.1, 2.0]	1
	$\phi$	0.7	arc			
	$\alpha_0$	[0.4, 1.4]	1	$\alpha_1$	[0.4, 1.4]	1
on-fault	$b$	0.014	1	$L$	0.2	m
	$f_0$	0.6	1	$V_0$	$1.0 \times 10^{-6}$	m/s
	$f_w$	0.1	1	$V_w$	$1.0 \times 10^{-1}$	m/s
	$V_{init}$	$1.0 \times 10^{-16}$	m/s			

In our models, we fix  $b = 0.014$  and vary  $a$  to control the value of  $(a - b)$ . As a reference, we adopt the depth-dependent profile of  $a_0(z)$  from Taufiqurrahman et al. (2023), where  $z$  is the upward-positive depth coordinate (Fig. 1b). To parameterize spatial variability in the inversion, we introduce a scalar scaling factor  $\alpha$  and define depth-dependent  $a(z)$  as:

$$a(z) = \alpha a_0(z). \quad (1)$$

In the fast velocity-weakening formulation of rate-and-state friction (Dunham et al., 2011) that we use, fracture energy is primarily governed by the slip-weakening distance and the effective strength drop, the latter controlled by the frictional parameter combination  $a - f_w$ . This contrasts with the classical aging and slip laws, where the frictional strength drop is determined by  $b$  alone and is independent of  $a$  (?).

### 2.2.3. Inelastic off-fault deformation and initial stress

The off-fault nonlinear parameters in our model control inelastic deformation in bulk materials during earthquake rupture. We adopt a Drucker-Prager visco-elasto-plastic rheology (Andrews, 2005) to model off-fault inelastic deformation. Inelastic deformation accumulates when the shear stress exceeds a yield strength  $\tau_c$ , defined as

$$\tau_c = c \cos(\phi) - \sigma_p \sin(\phi), \quad (2)$$

where  $c$  is plastic cohesion,  $\phi$  is the bulk friction angle, and  $\sigma_p = \sigma_{kk}/3$  is the deviatoric mean normal stress given by the trace of the stress tensor  $\sigma_{ij}$ . The plastic cohesion  $c$  and internal friction angle  $\phi$  control the amount of inelastic off-fault deformation and strongly influence the rupture dynamics and the near-field ground motions.

We use the same multi-scale initial stress field as Taufiqurrahman et al. (2023), combining a 2D community stress model representing the regional stress state in the upper crust of Southern California with 3D Coulomb stress changes due to past regional earthquakes. The initial on-fault stress state are shown in Fig. S2 and the regional maximum horizontal stress orientation  $SH_{\max}$  in Fig. S3. The fault system is embedded in a geologically heterogeneous region, with 3D spatially varying rock elastic moduli based on a 3D community velocity model CVM-S4.26 (Lee et al., 2014). The plastic cohesion  $c(x, y, z)$  is proportional to shear modulus  $\mu(x, y, z)$  and changes in space according to the 3D community velocity model. We define the plastic cohesion as

$$c = \gamma_r \gamma \mu(x, y, z), \quad (3)$$

where  $\gamma$  is a scaling factor to be inferred during the inversion, and  $\gamma_r = 10^{-4}$  (Roten et al., 2014).

In the reference model which uses a spatially uniform on-fault direct-effect scaling parameter  $\alpha = 1$  in Eq. (1) and off-fault plastic cohesion scaling factor  $\gamma = 1$  in Eq. (3), an overshoot is observed in the southeastern segment of fault F1 when comparing to the surface displacement of GNSS stations and the fault-parallel offset data. To examine whether we can discriminate between on-fault and off-fault nonlinear processes that potentially suppress the overshoot of surface fault offset at the southeastern segment of the fault F1, we assume that the on-fault parameter  $\alpha$  and the off-fault parameter  $\gamma$  are both spatially variable along the fault strike direction, and that such variability allows for the modeled fault slip in dynamic rupture simulations to closer match observations. For simplicity, we assume that this

variation in  $a$  and  $\gamma$  along the southeastern segment of fault F1 is linear, and that scaling factors remain constant along the northwestern segment (Fig. 1a). Along the southeastern segment, the scaling factor of the direct-effect parameter  $a$  varies from  $\alpha_0$  to  $\alpha_1$ ; and for the scaling factor of plastic cohesion  $c$  from  $\gamma_0$  to  $\gamma_1$ . We will discuss this assumption in Section 4.1.

### 2.3. Bayesian inversion of large-scale dynamic rupture simulations

This section describes how we combine data with three different formats in the inversion framework (Section 2.3.1). Then, we formulate the Bayesian inverse problem with detailed explanations on how the covariance matrix in the data likelihood is designed (Section 2.3.2).

#### 2.3.1. Data space

We allow for spatial variation of plastic cohesion  $c$  and direct-effect parameter  $a$  in the southeastern part of the fault system, via respective scaling factors  $\gamma$  and  $\alpha$  (Section 2.2). This results in a higher model flexibility, thus, a lower epistemic uncertainty, in the southeastern part of fault F1. To account for this in the data likelihood function (Section 2.3.2), we separate the fault-parallel offsets from the satellite images  $\Delta u^{obs}(s)$  into  $\Delta u^{NW,obs}(s)$  for  $s \leq 10$  km, and  $\Delta u^{SE,obs}(s)$  elsewhere, as shown by the dashed black axis in Fig. 1a. We define this first type of the data for  $\Delta u^{NW,obs}(s)$  and  $\Delta u^{SE,obs}(s)$ , respectively, as  $\mathbf{d}^{NW}$  and  $\mathbf{d}^{SE}$  in the Bayesian inversion with the following spatial discretization:

$$\mathbf{d}^{k,obs} = d_l^{k,obs} = \Delta u^{k,obs}(s_l), \quad k = NW \text{ or } SE, \quad (4)$$

where  $l$  runs from 1 to  $N^{NW}$  and  $N^{SE}$ , respectively, for the northwestern and southeastern parts of the fault.  $N^{NW} = 53$  and  $N^{SE} = 33$  are the numbers of along-strike discretization points  $s_l$ , at which the northwestern- and southeastern-segment fault-parallel offset values are measured.

Then, we define the second data type, the displacement time series  $u_i^{GT}(t)$  at 10 high-rate GNSS stations, as  $\mathbf{d}^{GT,obs}$  in the Bayesian inversion with the following temporal discretization:

$$\mathbf{d}^{GT,obs} = d_{il}^{GT,obs} = u_i^{GT,obs}(t_l), \quad i = 1, 2, \dots, n^{GT}, \quad (5)$$

where  $l$  runs from 1 to  $N^{GT} = 40$ , which is the number of discretized time steps  $t_l$  with a sampling rate of 1 Hz. The simulation duration is 40 s and  $n^{GT} = 3 \times 10$  is the total number of the three-component high-rate displacement time series.

The third type of data consists of the two horizontal components of static surface displacement  $u_j^{GS}$  at 11 GNSS stations. We define  $\mathbf{d}^{GS}$  as

$$\mathbf{d}^{GS,obs} = d_j^{GS,obs} = u_j^{GS,obs}, \quad j = 1, 2, \dots, n^{GS}, \quad (6)$$

where  $n^{GS} = 2 \times 11$  is the total number of static displacement measurements.

In summary, the complete data vector  $\mathbf{d}^{obs}$  that consists of the above three types of surface displacement measurement is defined as

$$\mathbf{d}^{obs} = (\mathbf{d}^{NW,obs}, \mathbf{d}^{SE,obs}, \mathbf{d}^{GT,obs}, \mathbf{d}^{GS,obs})^T, \quad (7)$$

with a total dimension of  $n_d = N^{NW} + N^{SE} + N^{GT} n^{GT} + n^{GS} = 1308$ .

#### 2.3.2. Data likelihood in Bayesian inversion

In Bayes' theorem, the model parameters  $\mathbf{m} = (\alpha_0, \alpha_1, \gamma_0, \gamma_1)^T$  and the experimental observations  $\mathbf{d}^{obs}$  defined in Eq. (7) are treated as random variables in  $\mathbb{M} \subset \mathbb{R}^{n_m}$  and  $\mathbb{D} \subset \mathbb{R}^{n_d}$ , respectively, where  $n_m$  and  $n_d$  denote the number of model parameters and the number of observed data points. Let  $G : \mathbb{M} \rightarrow \mathbb{D}$  be the model map that transforms a parameter set into a model prediction. Then, we aim to find the posterior probability density function (PDF),  $\rho(\mathbf{m}|\mathbf{d}^{obs})$ , which describes the conditional distribution of  $\mathbf{m}$  for a given observation  $\mathbf{d}^{obs}$ . We detail its relation to the model prior density  $\rho(\mathbf{m})$  and the data likelihood  $\rho(\mathbf{d}^{obs}|\mathbf{m})$  that describes the probability of measuring the observed data given one set of  $\mathbf{m}$  in Text S5. We focus in the following on the definition and formulation of the data likelihood  $\rho(\mathbf{d}^{obs}|\mathbf{m})$ .

We assume a zero-centered, additive Gaussian noise model for the observed data. It follows that the likelihood  $\rho(\mathbf{d}^{obs}|\mathbf{m})$  is given by:

$$\rho(\mathbf{d}^{obs}|\mathbf{m}) \propto \exp\left(-\frac{1}{2}(\mathbf{d}^{obs} - G(\mathbf{m}))^T \mathbf{C}^{-1}(\mathbf{d}^{obs} - G(\mathbf{m}))\right). \quad (8)$$

The covariance matrix  $\mathbf{C} \in \mathbb{R}^{n_d \times n_d}$  encapsulates the statistics of the noise, reflecting both measurement precision and epistemic uncertainties due to model assumptions. Given the modest dimensionality of our model space,  $\dim(\mathbb{M}) = 4$ , we assume that the diagonal components of the covariance matrix  $\mathbf{C}$  exceed their respective measurement uncertainties for the fault-parallel offsets, as well as high-rate and static GNSS displacement data.

As described in Section 2.2, the linear spatial variation in model parameters provides greater flexibility for the parameters governing dynamic rupture of the southeastern segment of fault F1. We assume this reduces epistemic uncertainty in that segment. Consequently, we assign different standard deviations for point-wise measurements of the fault-parallel offset,  $\sigma_i^{SE} = 0.6$  m for the southeastern segment and  $\sigma_j^{NW} = 0.84$  m for the northwestern segment. Since the epistemic uncertainty resulting from the limited model dimensionality ( $n_m = 4$ ) is difficult to quantify precisely, we discuss the sensitivity of the inversion results to the choice of likelihood function in Text S6 and Fig. S5.

Similarly, we assign  $\sigma_k^{GT}$  values ranging from 4 cm to 12 cm for the high-rate GNSS time series (GT), such that the misfit between the reference model and the data is  $\approx 2\sigma_k^{GT}$  (Table S1). For the static horizontal GNSS displacements, we set  $\sigma_l^{GS} = 1$  cm for each component, which is 5 $\times$  the reported observed data precision (Floyd et al., 2020). We assume that all observations are statistically independent and define the diagonal covariance matrix in blocks as:

$$\mathbf{C} = \text{diag}(\boldsymbol{\Sigma}^{NW}, \boldsymbol{\Sigma}^{SE}, \boldsymbol{\Sigma}^{GT}, \boldsymbol{\Sigma}^{GS}), \quad (9)$$

where  $\boldsymbol{\Sigma}^{NW} = \Sigma_i^{NW} = N^{NW}(\sigma_i^{NW})^2$ ,  $\boldsymbol{\Sigma}^{SE} = \Sigma_j^{SE} = N^{SE}(\sigma_j^{SE})^2$ ,  $\boldsymbol{\Sigma}^{GT} = \Sigma_k^{GT} = N^{GT}(\sigma_k^{GT})^2$ , and  $\boldsymbol{\Sigma}^{GS} = \Sigma_l^{GS} = (\sigma_l^{GS})^2$  are four vectors of variances with lengths of  $N^{NW}$ ,  $N^{SE}$ ,  $N^{GT}$ , and  $n^{GS}$ , respectively.

The posterior density  $\rho(\mathbf{m}|\mathbf{d}^{obs})$  can be computed point-wise up to an unknown constant factor  $\rho(\mathbf{d}^{obs})$ . Each sample thus requires an evaluation of the model map  $G(\mathbf{m})$ , i.e., a dynamic rupture simulation. Since each such simulation can be computationally expensive, we employ the MLDA algorithm detailed in the following, which ensures efficient sampling of the posterior using a hierarchy of approximate and high-fidelity simulations.

## 2.4. Hierarchical Bayesian Sampling via MLDA with Prefetching

Building on the MCMC sampling method (Hastings, 1970), the MLDA algorithm achieves computational efficiency by combining many fast approximate models with a small number of fully resolved simulations to correct for approximation errors. A major drawback of traditional MCMC methods (e.g., Cui et al., 2016) is their requirement for a large number of forward model evaluations to obtain sufficiently uncorrelated samples of the target posterior density  $\pi$ . To reduce the number of costly evaluations, we employ the MLDA algorithm (Lykkegaard et al., 2023) with a three-level model hierarchy. MLDA employs MCMC sampling on low-cost approximate models to produce high-quality proposals for MCMC sampling steps on more accurate, computationally intensive levels.

Our model hierarchy consists of a Gaussian process regression (GPR, Schulz et al., 2018) surrogate model at the coarsest level  $l = 1$ . This surrogate model guides the sampling process by proposing mostly decorrelated samples for the finer (higher-resolution) levels ( $l = 2, 3$ ) at very low computational cost. For the results presented in Section 3, we train the surrogate model using 87 SeisSol simulations at level  $l = 3$  with parameters randomly selected in the model space  $\mathbb{M}$ , enabling it to map the input model parameters  $\mathbf{m}$  to likelihood estimates in Eq. (8). The models at levels  $l = 2$  and  $l = 3$  both use high-resolution SeisSol simulations on computational meshes with approximately 4 million tetrahedral elements (Sec. 2.2.1). SeisSol's polynomial degree of the basis functions is set to two on level  $l = 2$  and three on level  $l = 3$ . Between two accepted samples at level  $l = 3$ , we evaluate two samples at level  $l = 2$ , along with an additional 60 samples at level  $l = 1$ . This multilevel scheme can reduce the autocorrelation between samples by up to 90% at the finest level ( $l = 3$ ), allowing posterior estimation with drastically reduced numbers of expensive simulations. In addition, we implement a prefetching technique (Angelino et al., 2014) within MLDA to improve scalability on supercomputers. Prefetching enables a parallel speedup of up to four times by simultaneously running multiple candidate simulations within each parallel Markov chain (Kruse et al., 2025).

## 2.5. Computational cost

We perform the inversion using the prefetching MLDA implementation of Kruse et al. (2025), interfaced through UM-Bridge (Seelinger et al., 2023) to control simulation runs on the Frontera supercomputer (Stanzione et al., 2020). Frontera is equipped with Intel Xeon Platinum 8280 ("Cascade Lake") processors, each with 56 cores per node operating at 2.7 GHz. The total number of available compute nodes is 8368. On this machine, SeisSol models at levels  $l = 2$  and  $l = 3$  require approximately 20 and 10 node hours per simulation, respectively. The GPR surrogate model at level  $l = 1$  costs  $< 1$  s in each model evaluation.

For this inversion, we utilized 4096 Frontera nodes for  $\sim 19$  hours, resulting in a total computational cost of 4,358,144 CPUh. Increasing the resolution of the highest-fidelity forward model would substantially increase the computational demands. For example, increasing the degree of polynomial basis functions from 3 to 4 would increase the computational cost by a factor of 7.

## 3. Results

We present Bayesian inference results for linearly varying off-fault plastic cohesion ( $\gamma_0, \gamma_1$ ) and on-fault direct-effect parameter in SVW-RS friction ( $\alpha_0, \alpha_1$ ). Following Kruse et al. (2025), we optimize the configuration of the MLDA hierarchy to maximize the number of effective posterior samples. Using 16 MLDA chains with two prefetching threads each, and running SeisSol in parallel on 4096 nodes, we generate a total of 912 samples on the finest level. To mitigate initialization bias in estimating the Bayesian posterior  $\rho(\mathbf{m}|\mathbf{d}^{obs})$  (Eq. (8) in the SI), we discard the first 20 samples in each Markov chain as "burn-in", based on analysis of the autocorrelation functions (Fig. S6a) and rank-normalized  $\hat{R}$ -statistics (Fig. S6b, Vehtari et al., 2021) of the MLDA chains. After excluding the "burn-in" phase samples, 592 effective samples remain.

Rupture dynamics in all preferred models closely resemble those of the observationally validated reference model (SI Text S1, Movie S1), with some differences including reduced shallow peak slip rates and reduced slip on the secondary fault segment F2 (Fig. S7). In our strongly velocity-weakening regime, and with limited off-fault deformation, co-seismic slip is governed primarily by the dynamic stress drop. Thus, because prestress is held fixed throughout the inversion, the modeled slip at depth remains nearly constant across the model space.

### 3.1. Posterior distributions of on- and off-fault parameters

We estimate the 1D and 2D posterior probability density of the model parameters from the effective MLDA samples (Fig. 2). Models with a posterior probability density  $\rho(\mathbf{m}|\mathbf{d}^{obs}) > 0.5\rho_{max}$  are marked by yellow squares, where  $\rho_{max}$  is the maximum posterior probability density of the best-fit model. In the following, we refer to these as "preferred models".

These preferred models cluster in regions of high model posterior density (dark blue shading), confirming that the MLDA chains adequately sample the posterior distribution  $\rho(\mathbf{m}|\mathbf{d}^{obs})$ . The mean values among the preferred models are  $\gamma_0 \approx 0.6$  and  $\gamma_1 \approx 0.7$ , corresponding to, respectively,  $6.0 \times 10^{-5} \mu(x, y, z)$  for the northwestern plastic cohesion and  $7.0 \times 10^{-5} \mu(x, y, z)$  for the plastic cohesion around the southeastern ends of the fault system (Fig. 1). These values are consistent with the peaks of the 1D marginal distributions (Fig. 2a, f).

Similarly, the mean on-fault direct-effect parameters are  $\alpha_0 \approx 0.8$  in the northwest and  $\alpha_1 \approx 1.2$  in the southeast (dark blue region, Fig. 2l). Below 4 km depth, this corresponds to a linear increase in  $(a - b)$  from -0.006 to -0.002 along fault F1, indicating spatially varying velocity-weakening behavior with less weakening occurring during dynamic rupture in the southeast.

The estimated posterior density reveals information on the trade-offs and correlations between off-fault plastic cohesion and on-fault direct-effect parameter in explaining surface displacement observations. In the northwestern F1 segment, the 2D marginal posterior distribution of  $\gamma_0$  and  $\alpha_0$  shows a clear positive correlation (Fig. 2c), which suggests that locally smaller off-fault inelastic deformation (larger  $\gamma_0$ ) can be partially compensated by reduced velocity-weakening frictional behavior (larger  $\alpha_0$ ). In contrast, no such correlation exists in the southeastern segment of the fault (Fig. 2h). In the southeastern segment, preferred models are concentrated around  $\gamma_1 \approx 0.7$  and  $\alpha_1 \approx 1.2$ , indicating that both increased off-fault inelastic deformation and reduced velocity-weakening friction are required to suppress the local offset overshoot seen in the reference model.

To validate consistency with the surrogate model, we compare the MLDA posterior density estimates to the data likelihood  $\rho(\mathbf{d}^{obs}|\mathbf{m})$  computed for the 87 samples (red dots in the sub-diagonal panels of Fig. 2) used to pre-train the



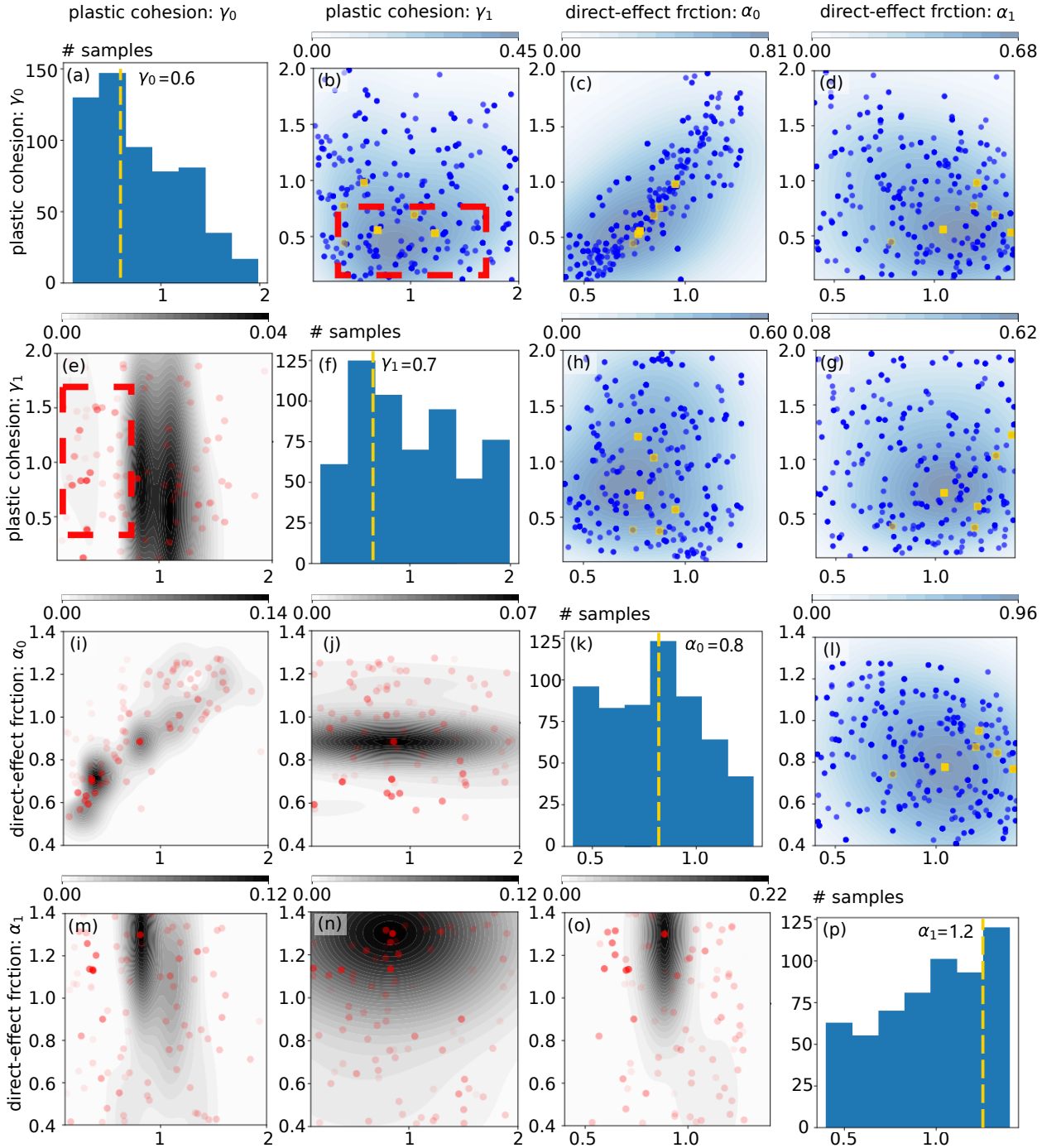


**Figure 2:** Panels of the Bayesian likelihood  $\rho(\mathbf{d}^{obs}|\mathbf{m})$  from the pretrained surrogate model and the Bayesian posterior  $\rho(\mathbf{m}|\mathbf{d}^{obs})$  from the MLDA inversion. The diagonal panels (from top to bottom) show the 1D marginal posterior probabilistic distributions of the off-fault plastic cohesion ( $\gamma_0$ ,  $\gamma_1$ ) and the on-fault direct-effect parameters in SVW-RS friction ( $\alpha_0$ ,  $\alpha_1$ ). The super-diagonal panels show the 2D marginal Bayesian posterior distributions for each parameter pair inferred from the MLDA inversion. The blue dots are all effective samples from the 16 Markov chains. The density of the dots is color-coded in blue, proportional to the posterior  $\rho(\mathbf{m}|\mathbf{d}^{obs})$ . The density color-code is computed using a Gaussian kernel density estimator (Kristan et al., 2011). The sub-diagonal panels show the 2D marginal Bayesian likelihoods as computed by the surrogate model, color-coded in gray. Red dots are the 87 samples used to pretrain the surrogate model; darker reds correspond to samples with higher likelihood  $\rho(\mathbf{d}^{obs}|\mathbf{m})$ .

GPR model. High-density MLDA posterior regions (highlighted by the dashed red rectangle in Fig. 2c) overlap with the high-likelihood surrogate training points (dots with darker red color in Fig. 2i).

The simple pre-trained surrogate model at level  $l = 1$  (color-coded in gray in the sub-diagonal panels of Fig. 2) is allowed to under-represent the probability distribution. For example, the surrogate model misses the local high-probability density region in Fig. 2e (dashed red rectangle) that is recovered by the MLDA inversion (Fig. 2b). This highlights an key benefit of our multilevel approach: approximate models accelerate inference, while the final results retain the accuracy of high-resolution 3D dynamic rupture simulations.

### 3.2. Surface displacement and uncertainty from preferred models

Models from the MLDA chains provide two types of information on how well the simulations explain observed surface ground displacement. First, similar to deterministic inversion approaches, the preferred models reduce the misfits between the model predictions and the observations. Second, enabled by the Bayesian framework, the ensemble of MLDA samples quantifies uncertainties in the predicted surface displacements.

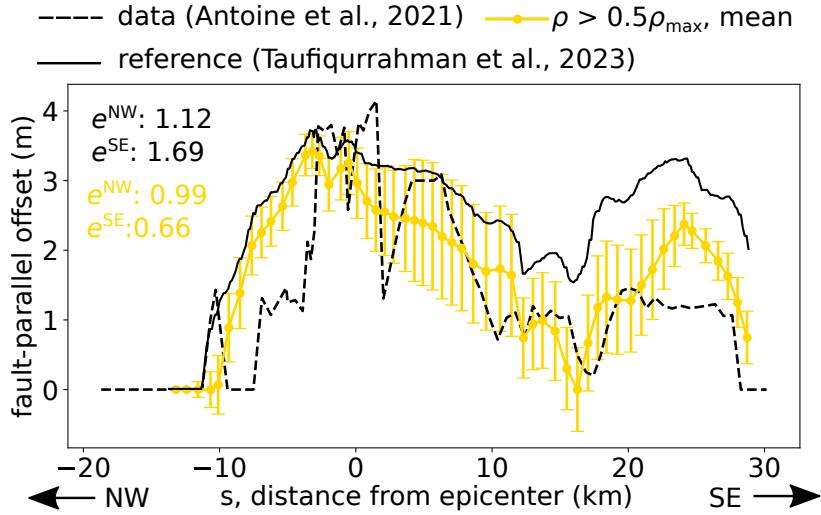


**Figure 3:** Fault-parallel offsets from model parameterizations with high posterior probability density. The yellow curve shows the mean offsets of the models with posterior probability density  $\rho(\mathbf{m}|\mathbf{d}^{obs}) \geq 0.5\rho_{max}$ .  $\rho_{max}$  is the maximum posterior density  $\rho(\mathbf{m}|\mathbf{d}^{obs})$  among all models from the 16 MLDA chains. Error bars show the standard deviation of the modeled offsets among all MLDA models. The dashed black curve shows observed fault-parallel offset data from Antoine et al. (2021), and the solid black curve shows the modeled offsets from the reference dynamic rupture model of Taufiqurrahman et al. (2023) in the solid black curve. The numbers are the misfits between the data and our preferred modeled offsets in the northwest ( $e^{NW}$ ) and southeast ( $e^{SE}$ ) of the fault in meters, as defined in Eqs. (10) and (11). The colors of the numbers correspond to those of the solid curves.

The preferred models reduce the fault-parallel offset overshoot in the southeastern part of fault F1 ( $s = 10 - 30$  km, Fig. 3) by 42% compared to the reference model. The peak offset is reduced from 3.2 m to  $\sim 2.4$  m (yellow curve). The standard deviation of the modeled fault-parallel offsets ranges from 0.2 to 0.9 m, consistent with the standard deviations  $\sigma_i^{SE} = 0.6$  m and  $\sigma_i^{NW} = 0.84$  m used in the data likelihood  $\rho(\mathbf{d}^{obs}|\mathbf{m})$  in Eq. (8). The largest standard deviations occur between  $s = 5$  km and  $s = 20$  km, and cover the misfits between the preferred models and the data.

We define the normalized misfits  $e^{NW}$  and  $e^{SE}$  for the northwestern ( $s \leq 10$  km) and southeastern ( $s > 10$  km) segments as:

$$e^{NW} = \sqrt{\frac{(\mathbf{d}^{NW}(\mathbf{m}) - \mathbf{d}^{NW,obs})^T (\mathbf{d}^{NW}(\mathbf{m}) - \mathbf{d}^{NW,obs})}{N^{NW}}}, \quad (10)$$

$$e^{SE} = \sqrt{\frac{(\mathbf{d}^{SE}(\mathbf{m}) - \mathbf{d}^{SE,obs})^T (\mathbf{d}^{SE}(\mathbf{m}) - \mathbf{d}^{SE,obs})}{N^{SE}}}, \quad (11)$$

where  $\mathbf{d}^{NW}(\mathbf{m})$  and  $\mathbf{d}^{SE}(\mathbf{m})$  are the modeled fault-parallel offsets for a given parameterization  $\mathbf{m}$ . Other variables are defined in Eq. (9).

The normalized misfit for the mean preferred models is  $e^{NW} = 0.99$  m (Fig. 3). This relatively large misfit may indicate that additional small-scale spatial variability, particularly in plastic cohesion  $c$  or the direct-effect parameter  $a$ , could improve the fit. The large standard deviations in this region are consistent with this interpretation. Along the southern segment ( $s = -10$  km to  $s = 5$  km), however, the offsets show persistent data misfits not fully explained by variations in  $c$  and  $a$ . We imposed a linear variation of parameters to counter the overshoot of the reference model, but, because  $\alpha_1$  and  $\gamma_1$  describe only a limited part of the fault, they may contribute little weight to the misfit function, which in turn may explain the lack of trade-off observed between these parameters.

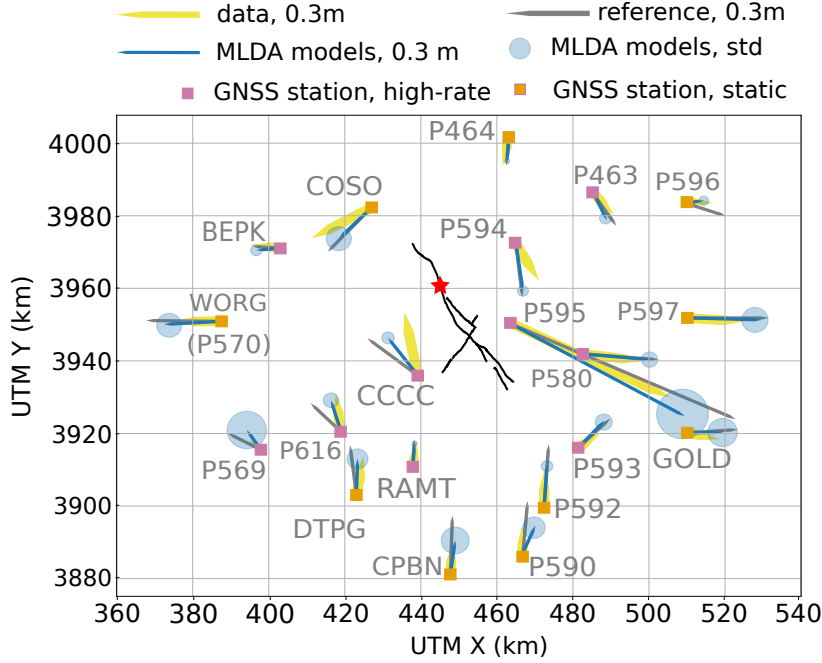


**Figure 4:** Co-seismic horizontal static displacements at 21 GNSS stations. Orange squares indicate stations used only for static displacement data, and pink squares mark those stations where high-rate displacement observations are available. Blue arrows show the mean modeled displacements from the preferred models, with circle radii equal to two times the standard deviation from the MLDA ensemble. Yellow arrows denote static GNSS displacement data from Floyd et al. (2020), and gray arrows denote results from the reference dynamic rupture model (Taufiqurrahman et al., 2023). The modeled and observed 40 s displacement time series at 10 high-rate stations are provided in Fig. S8.

Among the 21 GNSS stations used in our inversion, the observed static displacements fall within two standard deviations of the model predictions (Fig. 4, blue filled circles) at 14 of the 21 stations in the preferred models. This corresponds to a 45% reduction in misfit compared to the reference model. Specifically, our preferred models reduce the static displacement at most GNSS stations south of the faults (e.g., stations DTPG, P592, CPBN, Fig. 4). This reduction is due to the  $\approx 1.3$  m smaller cumulative fault slip and the smaller rupture area in our preferred models (Fig. 5a) compared to the reference model (Fig. S4a). Similarly to the fault-parallel offsets, discrepancies in displacements not covered by the model uncertainties indicate that a higher-dimensional parameter space may be required to match the spatial complexity of the rupture.

The preferred models (yellow dots in Fig. 2) match the observed seismic waveforms better than the reference model, primarily due to a  $\sim 30\%$  reduction in slip rate within the top 2 km of the fault (Movie S1) due to enhanced off-fault plastic yielding (Figs. S11, S12). For example, they reduce the velocity amplitudes at the seismic station CCC by  $\sim 55\%$  (Fig. S9). While the moment release rate of the preferred models retains the same mean moment magnitude ( $M_w = 6.98 \pm 0.01$ ) as the reference model, the second peak is lower (Fig. S10), in agreement with kinematic inversions (e.g., Goldberg et al., 2020).

### 3.3. Uncertainty in fault slip distribution and shallow slip deficit from dynamic rupture inversion

The ensemble of models from the MLDA chains allows us to derive the preferred fault slip distribution on fault F1 as well as to quantify its uncertainty. Figure 5a shows the mean cumulative slip from the preferred models, while Fig. 5b shows the corresponding standard deviation (std). A small fault segment (blue line in Fig. 5a), where the rupture does not reach the surface in the preferred models, corresponds to a location of incomplete surface rupture. The local prestress ratio (defined in Eq. (1) in the SI) is as low as 0.2 (Fig. S2b), reflecting the unfavorable orientation of this fault segment relative to the background stress. Unlike the reference model, the enhanced off-fault inelastic deformation dissipates enough energy to inhibit local rupture to the surface. This local lack of surface rupture is consistent with previous kinematic inversion results (Antoine et al., 2024). The largest fault slip uncertainties occur at shallow depths, within approximately  $\sim 3$  km of the surface, where standard deviations exceed 0.4 m. This is the depth range where on-fault friction transitions from velocity-weakening to velocity-strengthening (Fig. 1b), and where inelastic deformation becomes prominent, due to the shallowly reduced shear modulus (Fig. S11). Because plastic cohesion is assumed to decrease linearly with shear modulus, inelastic strain begins to accumulate at lower dynamic stress levels. Within this depth range, the fault slip between  $s = 5 - 20$  km along-strike exhibits the largest uncertainties, with standard deviations exceeding 0.7 m. These larger uncertainties align with large variations in fault-parallel offsets within the same along-strike region (Fig. 3). In contrast, the fault slip between  $s = 20$  km and  $s = 30$  km along-strike shows lower uncertainties, with standard deviations between 0.3 m and 0.4 m. Here, the variability reflects ambiguities in the location of rupture termination (blue circles, Fig. 5b). While the preferred models suggest rupture over a limited area of the fault system, the MLDA sampling does not exclude models with larger rupture extents.

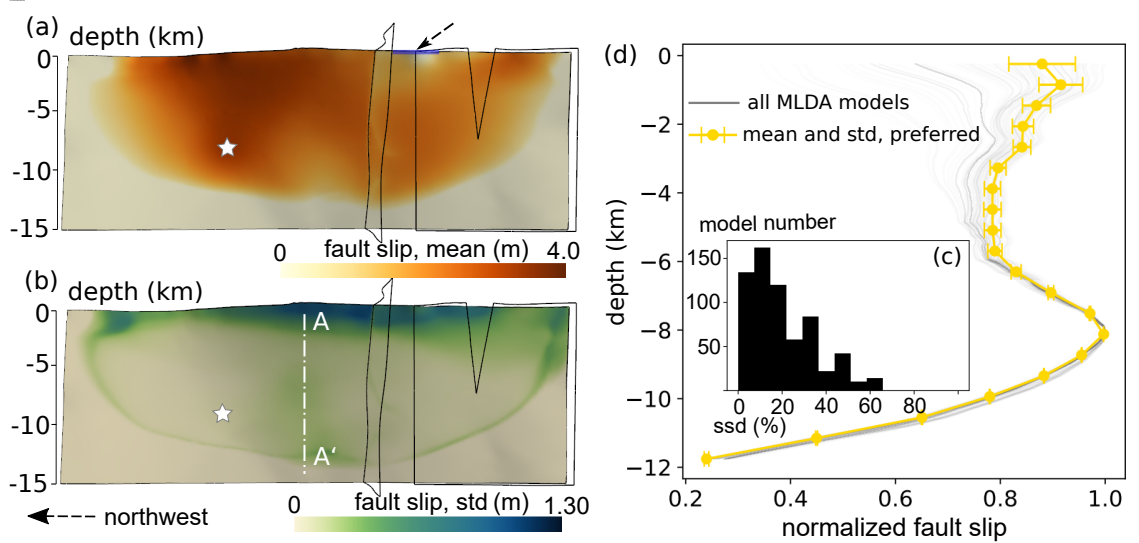


**Figure 5:** Uncertainties in fault slip distribution among all models in the MLDA chains. Panels (a) and (b) show, respectively, the mean and the standard deviation of fault slip. White stars mark the hypocenter where the dynamic rupture models prescribe earthquake nucleation. (c) Histogram of shallow slip deficits (SSDs) across all models. (d) Variation of fault slip with depth. The yellow curve shows the mean fault slip among the preferred models (yellow dots, Fig. 2), error bars show depth-dependent fault slip standard deviations. Gray curves show results from all accepted models. The off-fault inelastic deformation around the A-A' cross-section in (b) is shown in Fig. S11.

We use the MLDA ensemble to statistically evaluate the SSD from our physics-based dynamic rupture models (Fig. 5a). The SSD is commonly defined as the percentage of one minus the ratio of average fault slip at the surface to the maximum fault slip at depth (Fialko et al., 2005). As shown in Fig. 5c, more than 65% of the models exhibit low SSDs around a peak of  $\sim 10\%$ . The mean SSD among the preferred models is 13.1% (yellow curve and error bars in Fig. 5d) with a standard deviation of 5.1%. We observe that fault slip uncertainty increases toward shallower depths, consistent with the greater variability in modeled near-surface deformation.



## 4. Discussion

### 4.1. Trade-offs between off-fault plasticity and frictional weakening and implications for fault maturity and fault zone structure

Off-fault plastic cohesion ( $c$ , Eq. (2)) and on-fault rate-and-state friction parameters ( $a - b$ , Eq. (3) in the SI) jointly affect rupture dynamics and the resulting fault slip distribution and off-fault deformation (e.g., Biemiller et al., 2023). Our Bayesian inversion reveals trade-offs between off-fault plastic cohesion and on-fault frictional weakening specifically in the northwestern part of the fault system. This indicates that locally co-seismic surface deformation may be equally well explained by different combinations of inelastic and frictional properties, which reflects the competing roles of off-fault damage and fault weakening in dissipating earthquake energy. Plastic cohesion controls energy dissipation through off-fault inelastic deformation, competing with the energy loss from frictional heating in consuming the total energy released from the earthquake (Nielsen et al., 2016). On the other hand, ( $a - b$ ) influences the amount of energy dissipation during unstable fault slip (Dunham et al., 2011). The Bayesian inversion with MLDA enables us to investigate whether (and how) it is possible to discriminate the effects of  $c$  and ( $a - b$ ) on the on- and off-fault deformation from observed surface displacements, providing physical insights that extend beyond best-fit models.

In the southeastern part of the fault system, matching the observed fault-parallel offsets requires both enhanced inelastic deformation and reduced frictional weakening, suggesting that neither mechanism alone is sufficient. These spatial variations in the interplay of on-fault friction and off-fault damage may reflect along-strike variations in fault zone maturity. A supporting observation is the relatively discontinuous surface fault trace mapped along the southeastern part of fault F1 prior to the 2019 Ridgecrest earthquake (Thompson Jobe et al., 2020), which may suggest a less mature fault zone (Dolan and Haravitch, 2014; Manighetti et al., 2021), which is typically associated with less severe velocity-weakening (Ikari et al., 2011).

The reduced plastic cohesion favored by the inversion to match surface deformation may reflect the presence of a shallow fault zone surrounding the ruptured fault segments (e.g., Roten et al., 2017b). In the high-probability subset of the inversion (yellow squares, Fig. 2), lower plastic cohesion  $c$  is achieved by decreasing the scaling factor  $\gamma$  that relates it to the shear modulus  $\mu(x, y, z)$  (Eq. (3)). Imaging studies support this interpretation, having identified shallow fault zones, 3–5 km deep, surrounding the Ridgecrest rupture area (Qiu et al., 2021; Zhou et al., 2022), which considerably affects rupture dynamics and the resulting ground shaking (Yeh and Olsen, 2023; Schliwa et al., 2025). For example, Qiu et al. (2021) report a shallow waveguide with a 20% reduction in shear wave velocity relative to the surrounding host rock, corresponding to a  $\sim 36\%$  reduction in shear modulus, consistent with our preferred model values of  $\gamma_0 \approx 0.6$  and  $\gamma_1 \approx 0.7$ .

### 4.2. Uncertainty in shallow slip deficit and the role of inelastic deformation

We quantitatively compare the SSD inferred from our ensemble of dynamic rupture simulations with estimates from kinematic fault slip inversions (Wang et al., 2020), to assess whether observed SSDs can be reproduced. In the southeastern part of the fault system, lower plastic cohesion ( $\gamma_0$  and  $\gamma_1$ ) and less prominent velocity-weakening behavior (larger  $\alpha_1$ ) reduce the fault-parallel offset in our preferred models (yellow curve, Fig. 3). This reduced cohesion leads to more distributed off-fault inelastic deformation (Figs. S11, S12), which in turn increases the SSD.

Estimates of SSD from kinematic inversions range from 2% to 45%, reflecting large uncertainty (Ross et al., 2019; Goldberg et al., 2020; Wang et al., 2020; Antoine et al., 2024). It has been shown that assuming linear elastic rocks in kinematic inversions can overestimate SSD by 5%-25% (Ragon and Simons, 2021; Marchandon et al., 2021), suggesting that a more realistic range of SSD is between 8% and 32% (Antoine et al., 2024). From our Bayesian inversion,  $\sim 55\%$  of the MLDA samples fall within this SSD range, demonstrating that co-seismic off-fault deformation can quantitatively account for the observed SSD.

### 4.3. Toward higher-dimensional inversions

The primary limitation of our inversion is the limited dimensionality of the model space ( $n_m = 4$ ). As reflected in the choice of likelihood covariance matrix (Eq. (8)) and the misfits to the GNSS displacement time series (Fig. S8), this low dimensional parameterization increases epistemic uncertainties and limits the model's ability to match all observations within their measurement accuracies.

The uncertainty analysis suggests that smaller-scale variations in on-fault friction and off-fault plasticity, beyond the here imposed linear along-strike gradients, may improve to fit to observed fault offsets within measurement accuracy

(0.05 m), particularly in the range  $s = 5 - 20$  km. For  $s < 5$  km, however, we show that variations in  $c$  and  $a$  alone are insufficient, implying that additional complexity or physical parameters, especially at depths shallower than  $\sim 4$  km, may be required. Addressing these limitations would require higher model dimensions  $n_m$  to include more parameters with enhanced spatial flexibility at much higher computational costs (Sec 2.5).

Our results show that increasing model dimensions at depths deeper than  $\sim 4$  km could help to reduce residual misfits in GNSS data. Unlike the offset data, the GNSS displacement standard deviations in the likelihood function (Eq. (8)) are much smaller, on the order of a few centimeters, and closer to measurement accuracy. GNSS displacements are particularly sensitive to the deeper portions of the fault slip distribution (Antoine et al., 2024). Yet, in our preferred models, residuals at 7 stations (e.g., CCCC) remain outside the two standard deviation uncertainty range. Furthermore, the posterior standard deviations in fault slip at depths below  $\sim 4$  km are relatively small (mostly  $< 0.1$  m), implying that further improvements may require incorporating other physical parameters beyond  $c$  and  $a$  at depth.

Together, these findings suggest that combining the currently available geodetic data with high-performance computing, it may be feasible to invert for a higher-dimensional parameter space—including depth-dependent variations in  $a$  and  $c$ , and possibly additional parameters governing on- and off-fault rheology.

Generalizing our MLDA inversion framework to higher-dimensional models will require improvements in two aspects. First, improved surrogate models are needed at the coarsest level, capable of generalizing to broader parameter spaces and supporting more complex dynamic rupture scenarios. Promising approaches for dynamic rupture simulations include reduced-order models, such as interpolated proper orthogonal decomposition (Hobson et al., 2025), deep-learning-based methods, such as neural networks (Gong et al., 2025), Fourier neural networks (Tainpakdipat et al., 2025), and derivative-informed neural operators (O’Leary-Roseberry et al., 2024). Second, the number of required costly fine-level dynamic rupture simulations must remain tractable, ideally in the range of a few thousands. This can be achieved through function-space Bayesian inference frameworks (e.g., Stuart, 2010) or by leveraging accurate parametric derivatives computed via adjoint dynamic rupture simulations (Stiernström et al., 2024).

## 5. Conclusions

For the first time, this study demonstrates the feasibility of probabilistic, physics-based earthquake source inversion by integrating 3D dynamic rupture simulations including off-fault inelastic deformation with hierarchical Bayesian inference. Using the multilevel delayed acceptance Markov chain Monte Carlo (MLDA) method, accelerated with prefetching and surrogate models, we achieve efficient uncertainty quantification with costly dynamic rupture simulations. Applied to the 2019 Mw 7.1 Ridgecrest earthquake, our approach combines high-resolution geodetic datasets—fault-parallel offsets from satellite imagery, high-rate GNSS time series, and static GNSS displacements, to constrain coupled nonlinear processes of on-fault frictional weakening and off-fault inelastic deformation.

The inferred posterior distributions reveal strong trade-offs between on-fault frictional weakening (direct-effect parameter,  $a$ ) and off-fault plasticity (plastic cohesion,  $c$ ). In the northwest of the fault system, lower plastic cohesion can compensate for stronger velocity-weakening behavior, jointly controlling the rupture dynamics and surface deformation. The preferred models favor spatially variable dynamic weakening, with (a-b) increasing from -0.006 in the northwest to -0.002 in the southeast, consistent with geological evidence for lower fault maturity in the southeastern segment. A corresponding gradient in plastic cohesion from  $\gamma_0 \approx 0.6$  to  $\gamma_1 \approx 0.7$  improves agreement with observed surface displacements and is consistent with seismic imaging of shallow damage zones.

Our Bayesian inversion constrains the shallow slip deficit (SSD) to  $13.1\% \pm 5.1\%$  among the preferred models. Notably, 55% of all MLDA samples fall within the 8–32% SSD range estimated by previous kinematic inversions when accounting for off-fault deformation. This demonstrates that co-seismic inelastic processes are important to quantitatively explain the observed SSD. Our results provide new constraints on the maturity and shallow structure of the Ridgecrest fault system, and illustrate how joint inversion of on- and off-fault processes can improve our physical understanding of rupture mechanics. This study establishes an openly available HPC-empowered and physics-based framework for probabilistic earthquake source modeling that captures coupled nonlinearities in rupture dynamics and off-fault deformation. Our results pave the way for systematic exploration of fault zone properties, uncertainty quantification, and physics-based seismic hazard assessment.

## Acknowledgements

The authors thank Sebastian Wolf for his help with the implementation of the inversion scheme on the SuperMUC and Frontera supercomputers, Mathilde Marchandon for constructive comments and Yehuda Ben-Zion for fruitful discussions. This project has received funding from the Statewide California Earthquake Center (SCEC, project 25341), the Inno4scale project, which is funded by the European High Performance Computing Joint Undertaking (JU) under grant agreement No. 101118139, and from the European Union's Horizon 2020 research and innovation programme under the Marie-Sklodowska-Curie grant agreement No. 955515 – SPIN-ITN ([www.spin-itn.eu](http://www.spin-itn.eu)). This study was also supported by Horizon Europe (ChEESE-2P, grant number 101093038, DT-GEO, grant number 101058129, and Geo-INQUIRE, grant number 101058518), the National Science Foundation (grant numbers OAC-2139536, OAC-2311208, EAR-2225286, EAR-2121568), and the Deutsche Forschungsgemeinschaft (DFG, German Research Foundation, grant numbers 495931446, 518204048). We thank the Texas Advanced Computing Center (TACC) at the University of Texas at Austin for providing computational resources (project number EAR20006) that have contributed to the research results reported in this paper (<http://www.tacc.utexas.edu>). We also acknowledge the Gauss Centre for Supercomputing e.V. ([www.gauss-centre.eu](http://www.gauss-centre.eu)) for providing computing time on the supercomputer SuperMUC-NG at the Leibniz Supercomputing Centre ([www.lrz.de](http://www.lrz.de)) in project pn49ha. Additional computing resources were provided by the Institute of Geophysics of LMU Munich (Oeser et al., 2006).

## CRedit authorship contribution statement

**Zihua Niu:** Data curation, Formal analysis, Investigation, Methodology, Writing – original draft. **Maximilian Kruse:** Methodology, Software, Investigation, Visualization, Writing – review & editing. **Linus Seelinger:** Methodology, Software, Funding acquisition, Writing – review & editing. **Nico Schliwa:** Methodology, Validation, Writing – review & editing. **Heiner Igel:** Funding acquisition, Supervision, Writing – review & editing. **Alice-Agnes Gabriel:** Conceptualization of this study, Investigation, Methodology, Resources, Funding acquisition, Supervision, Validation, Writing – original draft.

## References

- Andrews, D.J., 2005. Rupture dynamics with energy loss outside the slip zone. *Journal of Geophysical Research: Solid Earth* 110. doi:<https://doi.org/10.1029/2004JB003191>.
- Angelino, E., Kohler, E., Waterland, A., Seltzer, M., Adams, R.P., 2014. Accelerating MCMC via parallel predictive prefetching. *arXiv preprint arXiv:1403.7265*.
- Antoine, S.L., Klinger, Y., Delorme, A., Wang, K., Bürgmann, R., Gold, R.D., 2021. Diffuse deformation and surface faulting distribution from submetric image correlation along the 2019 Ridgecrest, California, ruptures. *Bulletin of the Seismological Society of America* 111, 2275–2302.
- Antoine, S.L., Klinger, Y., Wang, K., Bürgmann, R., 2024. Coseismic shallow slip deficit accounted for by diffuse off-fault deformation. *Geophysical Research Letters* 51, e2024GL110798.
- Barbot, S., Lapusta, N., Avouac, J.P., 2012. Under the hood of the earthquake machine: Toward predictive modeling of the seismic cycle. *Science* 336, 707–710.
- Biemiller, J., Gabriel, A.A., Ulrich, T., 2023. Dueling dynamics of low-angle normal fault rupture with splay faulting and off-fault damage. *Nature Communications* 14, 2352.
- Cakir, Z., Doğan, U., Akoğlu, A.M., Ergintav, S., Özpapak, S., Özdemir, A., Nozadkhalil, T., Çakir, N., Zabcı, C., Erkoç, M.H., et al., 2023. Arrest of the Mw 6.8 January 24, 2020 Elazığ (Turkey) earthquake by shallow fault creep. *Earth and Planetary Science Letters* 608, 118085.
- Cui, T., Law, K.J., Marzouk, Y.M., 2016. Dimension-independent likelihood-informed mcmc. *Journal of Computational Physics* 304, 109–137.
- Day, S.M., Dalguer, L.A., Lapusta, N., Liu, Y., 2005. Comparison of finite difference and boundary integral solutions to three-dimensional spontaneous rupture. *Journal of Geophysical Research: Solid Earth* 110.
- Di Toro, G., Hirose, T., Nielsen, S., Pennacchioni, G., Shimamoto, T., 2006. Natural and experimental evidence of melt lubrication of faults during earthquakes. *science* 311, 647–649.
- Dolan, J.F., Haravitch, B.D., 2014. How well do surface slip measurements track slip at depth in large strike-slip earthquakes? The importance of fault structural maturity in controlling on-fault slip versus off-fault surface deformation. *Earth and Planetary Science Letters* 388, 38–47.
- Dunham, E.M., Belanger, D., Cong, L., Kozdon, J.E., 2011. Earthquake ruptures with strongly rate-weakening friction and off-fault plasticity, part 1: Planar faults. *Bulletin of the Seismological Society of America* 101, 2296–2307.
- DuRoss, C.B., Gold, R.D., Dawson, T.E., Scharer, K.M., Kendrick, K.J., Akciz, S.O., Angster, S.J., Bachhuber, J., Bacon, S., Bennett, S.E., et al., 2020. Surface displacement distributions for the July 2019 Ridgecrest, California, earthquake ruptures. *Bulletin of the Seismological Society of America* 110, 1400–1418.
- Fialko, Y., Sandwell, D., Simons, M., Rosen, P., 2005. Three-dimensional deformation caused by the Bam, Iran, earthquake and the origin of shallow slip deficit. *Nature* 435, 295–299.
- Finzi, Y., Langer, S., 2012. Damage in step-overs may enable large cascading earthquakes. *Geophysical Research Letters* 39.

- Floyd, M., Funning, G., Fialko, Y., Terry, R., Herring, T., 2020. Survey and continuous GNSS in the vicinity of the July 2019 Ridgecrest earthquakes. *Seismological Research Letters* 91, 2047–2054.
- Gabriel, A.A., Ampuero, J.P., Dalguer, L., Mai, P.M., 2013. Source properties of dynamic rupture pulses with off-fault plasticity. *Journal of Geophysical Research: Solid Earth* 118, 4117–4126.
- Gabriel, A.A., Kurapati, V., Niu, Z., Schliwa, N., Schneller, D., Ulrich, T., Dorozhinskii, R., Krenz, L., Uphoff, C., Wolf, S., Breuer, A., Heinecke, A., Pelties, C., Rettenberger, S., Wollherr, S., Bader, M., 2025. SeisSol [software]. URL: <https://doi.org/10.5281/zenodo.15685917>, doi:10.5281/zenodo.15685917.
- Gabriel, A.A., Ulrich, T., Marchandon, M., Biemiller, J., Rekoske, J., 2023. 3D dynamic rupture modeling of the 6 February 2023, Kahramanmaraş, Turkey Mw 7.8 and 7.7 earthquake doublet using early observations. *The Seismic Record* 3, 342–356.
- Gallovič, F., Valentová, L., Ampuero, J.P., Gabriel, A.A., 2019. Bayesian dynamic finite-fault inversion: 2. Application to the 2016 Mw 6.2 Amatrice, Italy, earthquake. *Journal of Geophysical Research: Solid Earth* 124, 6970–6988.
- Goldberg, D.E., Melgar, D., Sahakian, V., Thomas, A., Xu, X., Crowell, B., Geng, J., 2020. Complex rupture of an immature fault zone: A simultaneous kinematic model of the 2019 Ridgecrest, CA earthquakes. *Geophysical Research Letters* 47, e2019GL086382.
- Gong, Z., Wang, Z., Liang, C., Nienkötter, A., Wang, J., Ren, C., Peng, X., 2025. Rupturenet2d, a deep neural network based surrogate for dynamic earthquake rupture simulation in two dimensions. *Journal of Geophysical Research: Solid Earth* 130, e2024JB030069.
- Harris, R.A., Barall, M., Aagaard, B., Ma, S., Roten, D., Olsen, K., Duan, B., Liu, D., Luo, B., Bai, K., et al., 2018. A suite of exercises for verifying dynamic earthquake rupture codes. *Seismological Research Letters* 89, 1146–1162.
- Hastings, W.K., 1970. Monte Carlo sampling methods using Markov chains and their applications. *Biometrika* 57, 97–109.
- Hauksson, E., Yoon, C., Yu, E., Andrews, J.R., Alvarez, M., Bhadha, R., Thomas, V., 2020. Caltech/USGS Southern California Seismic Network (SCSN) and Southern California Earthquake Data Center (SCEDC): Data availability for the 2019 Ridgecrest sequence. *Seismological Research Letters* 91, 1961–1970.
- Hobson, G.M., May, D.A., Gabriel, A.A., 2025. Quantifying the influence of fault geometry via mesh morphing with applications to earthquake dynamic rupture and thermal models of subduction. *arXiv preprint arXiv:2506.15892*.
- Ikari, M.J., Marone, C., Saffer, D.M., 2011. On the relation between fault strength and frictional stability. *Geology* 39, 83–86.
- Kaneko, Y., Avouac, J.P., Lapusta, N., 2010. Towards inferring earthquake patterns from geodetic observations of interseismic coupling. *Nature Geoscience* 3, 363–369.
- Kaneko, Y., Fialko, Y., 2011. Shallow slip deficit due to large strike-slip earthquakes in dynamic rupture simulations with elasto-plastic off-fault response. *Geophysical Journal International* 186, 1389–1403.
- Kristan, M., Leonardis, A., Škočaj, D., 2011. Multivariate online kernel density estimation with Gaussian kernels. *Pattern recognition* 44, 2630–2642.
- Kruse, M., Niu, Z., Wolf, S., Lykkegaard, M., Bader, M., Gabriel, A.A., Seelinger, L., 2025. Scalable Bayesian inference of large simulations via asynchronous prefetching multilevel delayed acceptance, in: *Proceedings of the Platform for Advanced Scientific Computing Conference*, pp. 1–13.
- Lee, E.J., Chen, P., Jordan, T.H., Maechling, P.B., Denolle, M.A., Beroza, G.C., 2014. Full-3-D tomography for crustal structure in southern California based on the scattering-integral and the adjoint-wavefield methods. *Journal of Geophysical Research: Solid Earth* 119, 6421–6451.
- Lykkegaard, M.B., Dodwell, T.J., Fox, C., Mingas, G., Scheichl, R., 2023. Multilevel Delayed Acceptance MCMC. *SIAM/ASA Journal on Uncertainty Quantification* 11, 1–30. URL: <https://doi.org/10.1137/22M1476770>, doi:10.1137/22M1476770, arXiv:<https://doi.org/10.1137/22M1476770>.
- Manighetti, I., Mercier, A., De Barros, L., 2021. Fault trace corrugation and segmentation as a measure of fault structural maturity. *Geophysical Research Letters* 48, e2021GL095372.
- Marchandon, M., Hollingsworth, J., Radiguet, M., 2021. Origin of the shallow slip deficit on a strike slip fault: Influence of elastic structure, topography, data coverage, and noise. *Earth and Planetary Science Letters* 554, 116696.
- Marone, C., 1998. Laboratory-derived friction laws and their application to seismic faulting. *Annual Review of Earth and Planetary Sciences* 26, 643–696.
- Melgar, D., Melbourne, T.I., Crowell, B.W., Geng, J., Szeliga, W., Scrivner, C., Santillan, M., Goldberg, D.E., 2020. Real-time high-rate GNSS displacements: Performance demonstration during the 2019 Ridgecrest, California, earthquakes. *Seismological Research Letters* 91, 1943–1951.
- Mikumo, T., Hirahara, K., Miyatake, T., 1987. Dynamical fault rupture processes in heterogeneous media. *Tectonophysics* 144, 19–36.
- Nielsen, S., Spagnuolo, E., Violay, M., Smith, S., Di Toro, G., Bistacchi, A., 2016. G: Fracture energy, friction and dissipation in earthquakes. *Journal of seismology* 20, 1187–1205.
- Niu, Z., Gabriel, A.A., Ben-Zion, Y., 2025a. Delayed dynamic triggering and enhanced high-frequency seismic radiation from brittle rock damage in 3d dynamic rupture simulations. *Journal of Geophysical Research: Solid Earth* 130, e2025JB031632. URL: <https://agupubs.onlinelibrary.wiley.com/doi/abs/10.1029/2025JB031632>, doi:<https://doi.org/10.1029/2025JB031632>, arXiv:<https://agupubs.onlinelibrary.wiley.com/doi/pdf/10.1029/2025JB031632>. e2025JB031632 2025JB031632.
- Niu, Z., Gabriel, A.A., Wolf, S., Ulrich, T., Lyakhovsky, V., Igel, H., 2025b. A discontinuous galerkin method for simulating 3D seismic wave propagation in nonlinear rock models: Verification and application to the 2015 Mw 7.8 Gorkha earthquake. *Journal of Geophysical Research: Solid Earth* 130.
- Oeser, J., Bunge, H.P., Mohr, M., 2006. Cluster design in the earth sciences tethys, in: *International conference on high performance computing and communications*, Springer. pp. 31–40.
- O’Leary-Roseberry, T., Chen, P., Villa, U., Ghattas, O., 2024. Derivative-informed neural operator: an efficient framework for high-dimensional parametric derivative learning. *Journal of Computational Physics* 496, 112555.
- Peyrat, S., Olsen, K., 2004. Nonlinear dynamic rupture inversion of the 2000 Western Tottori, Japan, earthquake. *Geophysical research letters* 31.
- Premus, J., Gallovič, F., Ampuero, J.P., 2022. Bridging time scales of faulting: From coseismic to postseismic slip of the Mw 6.0 2014 South Napa, California earthquake. *Science advances* 8, eabq2536.



- Qiu, H., Ben-Zion, Y., Catchings, R., Goldman, M.R., Allam, A.A., Steidl, J., 2021. Seismic Imaging of the Mw 7.1 Ridgecrest Earthquake Rupture Zone From Data Recorded by Dense Linear Arrays. *Journal of Geophysical Research: Solid Earth* 126.
- Ragon, T., Simons, M., 2021. Accounting for uncertain 3-D elastic structure in fault slip estimates. *Geophysical Journal International* 224, 1404–1421.
- Ross, Z.E., Idini, B., Jia, Z., Stephenson, O.L., Zhong, M., Wang, X., Zhan, Z., Simons, M., Fielding, E.J., Yun, S.H., et al., 2019. Hierarchical interlocked orthogonal faulting in the 2019 Ridgecrest earthquake sequence. *Science* 366, 346–351.
- Roten, D., Olsen, K., Day, S., 2017a. Off-fault deformations and shallow slip deficit from dynamic rupture simulations with fault zone plasticity. *Geophysical Research Letters* 44, 7733–7742.
- Roten, D., Olsen, K., Day, S., Cui, Y., 2017b. Quantification of fault-zone plasticity effects with spontaneous rupture simulations. *Pure and Applied Geophysics* 174.
- Roten, D., Olsen, K., Day, S., Cui, Y., Fäh, D., 2014. Expected seismic shaking in Los Angeles reduced by San Andreas fault zone plasticity. *Geophysical Research Letters* 41, 2769–2777.
- Sambridge, M., 1999. Geophysical inversion with a neighbourhood algorithm—I. Searching a parameter space. *Geophysical journal international* 138, 479–494.
- Schliwa, N., Gabriel, A.A., Ben-Zion, Y., 2025. Shallow fault zone structure affects rupture dynamics and ground motions of the 2019 Ridgecrest sequence to regional distances. *Journal of Geophysical Research: Solid Earth* 130, e2025JB031194. doi:10.1029/2025JB031194.
- Schliwa, N., Gabriel, A.A., Premus, J., Gallovič, F., 2024. The linked complexity of coseismic and postseismic faulting revealed by seismo-geodetic dynamic inversion of the 2004 Parkfield earthquake. *Journal of Geophysical Research: Solid Earth* 129, e2024JB029410.
- Schulz, E., Speekenbrink, M., Krause, A., 2018. A tutorial on Gaussian process regression: Modelling, exploring, and exploiting functions. *Journal of mathematical psychology* 85, 1–16.
- Seelinger, L., Cheng-Seelinger, V., Davis, A., Parno, M., Reinartz, A., 2023. UM-Bridge: Uncertainty quantification and modeling bridge. *Journal of Open Source Software* 8, 4748. URL: <https://doi.org/10.21105/joss.04748>, doi:10.21105/joss.04748.
- Stanzione, D., West, J., Evans, R.T., Minyard, T., Ghattas, O., Panda, D.K., 2020. Frontera: The evolution of leadership computing at the National Science Foundation, in: *Practice and Experience in Advanced Research Computing 2020: Catch the Wave*, Association for Computing Machinery. pp. 106–111. URL: <https://doi.org/10.1145/3311790.3396656>, doi:10.1145/3311790.3396656.
- Stiernström, V., Almquist, M., Dunham, E.M., 2024. Adjoint-based inversion for stress and frictional parameters in earthquake modeling. *Journal of Computational Physics* 519, 113447.
- Stuart, A.M., 2010. Inverse problems: a Bayesian perspective. *Acta numerica* 19, 451–559.
- Tainpakdipat, N., Abdelmeguid, M., Zhao, C., Azizzadenesheli, K., Elbanna, A., 2025. Fourier Neural operators for accelerating earthquake dynamic rupture simulations. *Authorea Preprints*.
- Taufiqurrahman, T., Gabriel, A.A., Li, D., Ulrich, T., Li, B., Carena, S., Verdecchia, A., Gallovič, F., 2023. Dynamics, interactions and delays of the 2019 ridgecrest rupture sequence. *Nature* 618, 308–315.
- Thompson Jobe, J.A., Philipposian, B., Chupik, C., Dawson, T., K. Bennett, S.E., Gold, R., DuRoss, C., Ladinsky, T., Kendrick, K., Haddon, E., et al., 2020. Evidence of previous faulting along the 2019 Ridgecrest, California, earthquake ruptures. *Bulletin of the Seismological Society of America* 110, 1427–1456.
- Twardzik, C., Das, S., Madariaga, R., 2014. Inversion for the physical parameters that control the source dynamics of the 2004 Parkfield earthquake. *Journal of Geophysical Research: Solid Earth* 119, 7010–7027.
- Uphoff, C., Rettenberger, S., Bader, M., Madden, E.H., Ulrich, T., Wollherr, S., Gabriel, A.A., 2017. Extreme scale multi-physics simulations of the tsunamigenic 2004 Sumatra megathrust earthquake, in: *Proceedings of the international conference for high performance computing, networking, storage and analysis*, pp. 1–16.
- Vehtari, A., Gelman, A., Simpson, D., Carpenter, B., Bürkner, P.C., 2021. Rank-normalization, folding, and localization: An improved  $\hat{R}$  for assessing convergence of MCMC (with discussion). *Bayesian Analysis* 16, 667–718. doi:10.1214/20-BA1221.
- Wang, K., Dreger, D.S., Tinti, E., Bürgmann, R., Taira, T., 2020. Rupture process of the 2019 Ridgecrest, California Mw 6.4 foreshock and Mw 7.1 earthquake constrained by seismic and geodetic data. *Bulletin of the Seismological Society of America* 110, 1603–1626.
- Yeh, T.Y., Olsen, K.B., 2023. Fault damage zone effects on ground motions during the 2019 Mw 7.1 Ridgecrest, California, earthquake. *Bulletin of the Seismological Society of America* 113, 1724–1738.
- Zhou, Z., Bianco, M., Gerstoft, P., Olsen, K., 2022. High-resolution imaging of complex shallow fault zones along the July 2019 Ridgecrest ruptures. *Geophysical Research Letters* 49.

1 **Supporting Information for ”Constraining On- and**  
2 **Off-Fault Nonlinear Dynamic Rupture Parameters**  
3 **via Hierarchical Bayesian Inversion for the 2019 Mw**  
4 **7.1 Ridgecrest Earthquake”**

Zihua Niu<sup>1</sup>, Maximilian Kruse<sup>2</sup>, Linus Seelinger<sup>2</sup>, Nico Schliwa<sup>1</sup>, Heiner

Igel<sup>1</sup>, Alice-Agnes Gabriel<sup>4,1</sup>

5 <sup>1</sup>Department of Earth and Environmental Sciences, Ludwig-Maximilians-Universität München, Munich, Germany

6 <sup>2</sup>Scientific Computing Center, Karlsruhe Institute of Technology, Karlsruhe, Germany

7 <sup>3</sup>Department of Informatics, Technical University of Munich, Munich, Germany

8 <sup>4</sup>Scripps Institution of Oceanography, UC San Diego, La Jolla, CA, USA

9 **Contents of this file**

10 1. Caption for Movies S1

11 2. Text S1 to S10

12 3. Figures S1 to S12

13 4. Table S1

## Introduction

We apply the multi-level delayed acceptance (MLDA) algorithm to the the 2019  $M_w$  7.1 Ridgecrest earthquake, constraining the nonlinear parameters, i.e. on-fault rate-and-state friction parameters and off-fault plastic cohesion, in 3D dynamic rupture simulations with complex geometry. This supplementary file includes detailed information on the methods, model configurations, and results that are complementary to the main text. We show (1) model setup and resolution of the high-resolution reference model and the lowered-resolution models used in our inversion; (2) supporting results that demonstrate the reliability of our inversion results; (3) and differences between the reference model and our preferred model.

**Movie S1.** The movie compares the evolution of slip rate on the four fault segments between the preferred model (top panels) and the reference model (bottom panels) within 20 s after the mainshock onset.

## Text S1: Rupture dynamics of the reference model

The reference model by Taufiqurrahman et al. (2023) already explains a set of measurements from seismic stations, GNSS stations, satellite images, and field mapping. In the reference model (Fig. S1), the  $M_w$  6.4 Searles Valley foreshock nucleates at the 10.5 km depth close to the intersection of F3 and F4. Rupture on F3 is limited close to the nucleation point due to the non-optimal fault orientation, whereas the rupture on F4 reaches the ground surface. During the  $M_w$  7.1 Ridgecrest mainshock, the rupture initiates on F1 at a depth of 8 km. It first propagates as a bilateral crack on the northwestern part of F1. As the rupture front reaches the intersection of F4 and F1, a deep rupture pulse extends to the southeastern part of F1. The mainshock also dynamically triggers the rupture of

37 F2 at its southeastern end and reactivates slip on F4 near the intersection. For more  
 38 details please see Taufiqurrahman et al. (2023) and Schliwa & Gabriel (2023).

### 39 **Text S2: Fault structure and model setup**

40 We use the geometrically complex fault system geometry constructed by Taufiqurrah-  
 41 man et al. (2023), consisting of two subparallel faults (F1, F2, Fig. S2) ruptured in the  
 42  $M_w$  7.1 mainshock and two faults (F3, F4) that ruptured during the  $M_w$  6.4 foreshock.  
 43 F4 is also reactivated during the mainshock (Text S1). We first model 30 s of the  $M_w$   
 44 6.4 foreshock to account for its stress perturbations on the mainshock fault segments and  
 45 save the perturbed stress state. Then, we start modeling the  $M_w$  7.1 mainshock from the  
 46 saved stress state. The computational domain spans  $200 \text{ km} \times 200 \text{ km}$  horizontally with  
 47 a depth of 100 km, discretized with  $\sim 4.0$  million tetrahedral elements. The coordinate  
 48 system is calculated from the WGS84/UTM Mercator 11S projection (Fig. S3). The  
 49 surface topography is down-sampled from Farr et al. (2007) to a resolution of 1 km on  
 50 the free surface. The mesh around the faults is refined to a maximum element size of  
 51 200 m. With velocity-aware meshing (Breuer & Heinecke, 2022), ensuring at least six  
 52 elements per S-wave wavelength of a maximum target frequency (Käser et al., 2008), our  
 53 simulations resolve ground motions up to 1.0 Hz in the near-source region and up to 0.5  
 54 Hz in the rest of the domain. The simulations employ basis functions of polynomial order  
 55 2 and 3 at levels  $l = 2$  and  $l = 3$  in MLDA (Section 2.4 in the main text). The resolution  
 56 of our models does not facilitate matching every detail of the rupture dynamics of the  
 57 reference model. We compare our model resolution and results with those of the reference  
 58 model in Text S3.



The color code in Fig. S2 shows the distribution of the ratio of the potential stress drop to the reference strength drop (prestress ratio,  $R$ , Aochi & Madariaga, 2003; Schliwa et al., 2024), defined as

$$R = \frac{\tau - f_w \sigma_n}{(f_0 - f_w) \sigma_n}, \quad (1)$$

where  $\tau$  is the initial shear traction on the fault,  $\sigma_n$  is the effective normal stress that accounts for the pressurized fault zone fluids (Taufiqurrahman et al., 2023).  $f_w$  and  $f_0$  are SVW-RS friction parameters given in Table 1.  $R$  is a key parameter that controls the dynamic triggering potential of the fault (Kame et al., 2003).

### **Text S3: Effect of model resolution on inversion**

To ensure computational feasibility, the model resolution during inversion is reduced compared to the reference model, as only static displacement and low-frequency GNSS observations are important to constrain our inversion. The reference model uses a higher-resolution mesh, discretizing the same computational domain with  $\sim 27.2$  million tetrahedral elements. The mesh around the faults is refined to a maximum element size of 75 m. This mesh refinement is important to accurately determine the traction and slip rate changes within the rupture process zone, which is  $> 515$  m in 95% of the elements (Taufiqurrahman et al., 2023). The model resolves ground motions up to 2.0 Hz in the near-source region and up to 1.0 Hz in the rest of the domain. The high-resolution dynamic rupture model requires  $\sim 48$  times more CPU hours compared to our models at level  $l = 3$ , which is the most accurate model among the three levels of our prefetching MLDA algorithm. Because of the lower mesh resolution around the faults, our level-three model does not perfectly match the rupture dynamics, in terms of both fault slip and peak slip rate (Fig. S4). The

largest error in the fault slip is  $\sim 1.7$  m at the bottom of the ruptured area on fault F1. Local errors in the peak slip rate are also as significant as  $\sim 5$  m/s. The other region with noticeable errors in the peak slip rate ( $\sim 1.8$  m/s) is around the location of the rupture pulse on the southeastern part of F1 (Fig. S1). Here, the difference in fault slip is not as prominent ( $< 0.2$  m).

However, these differences in rupture dynamics between the reference model and our level-three model are not significant enough to influence our inversion accuracy. The resulting errors in our model outputs used to compare with the data in the inversion are below the standard deviations that we set in our Bayesian likelihood function in Eq. (8) in the main text. The greatest errors in static displacements at GNSS stations are the NS component of station P464 (5.8 mm, Table S1). However, this error is still below our assumed statistical uncertainties between the model outputs and the data (10 mm). The same conclusion applies for the GNSS stations recording high-rate displacement time series and fault-parallel offsets from satellite images.

In contrast, our level-two model is less accurate in terms of both rupture dynamics and model outputs, which is also not required for the accuracy of inversion with the MLDA algorithm (Kruse et al., 2025). This level-two model is only designed to help guide the sampling at level  $l = 3$ . The most significant errors in this model is that it terminates early and the rupture does not propagate along the southeastern segment of fault F1. This results in large differences in the peak slip rate ( $\sim 5$  m/s) and fault slip ( $\sim 3$  m). Such large errors in the rupture dynamics also contribute to larger errors in model outputs, compared to our assumed uncertainties between the model outputs and the data. For example, the assumed uncertainty in the fault offsets at  $s > 10$  km in the

along-strike coordinate is 600 mm, whereas the error between our level-two model and the high-resolution model is as large as 1323.1 mm.

#### **Text S4: SVW-RS friction law in dynamic rupture modeling**

We use this section to clarify the nonlinear parameters in the SV-RS friction law (Noda et al., 2009; Dunham et al., 2011) in Section 2.2.2 in the main text. In this friction law, the frictional fault strength  $\tau_s$  (the upper bound of the shear traction  $\tau$  on a fault surface) is proportional to the local normal traction  $\sigma_n$ , which is

$$\tau_s = f(V, \Psi)\sigma_n, \quad (2)$$

where  $f(V, \Psi)$  is known as the friction coefficient. It is a function of the slip rate  $V$  and the state variable  $\Psi$ . In SV-RS friction, it is defined as

$$f(V, \Psi) = a \sinh^{-1}\left(\frac{V}{2V_0} \exp\left(\frac{\Psi}{a}\right)\right), \quad (3)$$

where  $a$  is the direct-effect parameter and  $V_0$  is the reference slip rate, at which the friction coefficient takes a reference value  $f_0$ . The state variable  $\Psi$  evolves to its steady-state value  $\Psi_{ss}$  depending on the slip rate  $V$  and a characteristic slip distance  $L$  as

$$\frac{d\Psi}{dt} = -\frac{V}{L}(\Psi - \Psi_{ss}(V)), \quad (4)$$

where  $\Psi_{ss}(V)$  is written as

$$\Psi_{ss}(V) = a \ln\left(\frac{2V_0}{V} \sinh\left(\frac{f_{ss}(V)}{a}\right)\right), \quad (5)$$

corresponding to a steady-state friction coefficient  $f_{ss}$ . At steady state, the low-velocity friction coefficient  $f_{LV}$  is defined as

$$f_{LV}(V, \Psi) = f_0 - (b - a) \ln \frac{V}{V_0}, \quad (6)$$

where  $b$  is the evolution-effect parameter that determines how the friction evolves with the state variable  $\Psi$  from the instantaneous direct effect  $a$ . To account for the friction reduction at high slip rates, SV-RS friction further defines a fully weakened friction coefficient  $f_w$  at a weakened slip rate  $V_w$ . Combining  $f_{LV}$ ,  $f_w$  and  $V_w$ ,  $f_{ss}$  can be defined as

$$f_{ss}(V) = f_w + \frac{f_{LV}(V) - f_w}{(1 + (V/V_w)^8)^{1/8}}. \quad (7)$$

### Text S5: Mathematical description of the Bayesian inversion framework

To directly compute the posterior density  $\rho(\mathbf{m}|\mathbf{d}^{obs})$  of underlying parameters  $\mathbf{m}$  from the observed data, we would have to apply the inverse of the model map  $G^{-1}$ . However, that inverse is not available for our dynamic rupture models. Employing Bayes' theorem, we can reformulate the posterior in a way that, as will be detailed below, only involves the forward map  $G$ :

$$\rho(\mathbf{m}|\mathbf{d}^{obs}) = \frac{\rho(\mathbf{d}^{obs}|\mathbf{m})\rho(\mathbf{m})}{\rho(\mathbf{d}^{obs})} \propto \rho(\mathbf{d}^{obs}|\mathbf{m})\rho(\mathbf{m}), \quad (8)$$

where  $\rho(\mathbf{m})$  is the model prior density,  $\rho(\mathbf{d}^{obs}|\mathbf{m})$  is the likelihood that describes the probability density to measure the observed data when  $\mathbf{m}$  is given, and  $\rho(\mathbf{d}^{obs}) > 0$  is the unconditional PDF of measuring the observed data. In practice,  $\rho(\mathbf{d}^{obs})$  is inaccessible. MCMC methods circumvent this issue, in that they only require evaluations of the unnormalized density. Broadly speaking, the posterior  $\rho(\mathbf{m}|\mathbf{d}^{obs})$  takes higher values if a parameter is plausible from a-priori knowledge and its corresponding model prediction is close to the observed data. Importantly, the Bayesian framework permits and exposes model ambiguities (i.e., multiple different parameters explaining the observed data), gives a statistically meaningful uncertainty indication about how well given data constrain the

inferred parameters, and yields insights into how parameters could interact to reproduce the observation, which remains difficult (Wang et al., 2019).

The prior density  $\rho(\mathbf{m})$  encodes expert knowledge about what parameters might be generally plausible, without considering our specific observation. Taking into account physical constraints, we define an upper and a lower bound for the prior range of each value, as  $\mathbb{M} = \{\mathbf{m} \in \mathbb{R}^{n_m} | lb_i \leq m_i \leq ub_i, i = 1, 2, \dots, n_m\}$ .  $lb_i$  and  $ub_i$  are the assumed lower and upper bounds of each model parameter, as listed in Table 1. We assume that we know nothing about the parameters except their bounds. Therefore, based on the maximum entropy principle of designing the prior (Good, 1963), the most uninformative and therefore objective model prior is a uniform distribution in  $\mathbb{M}$ .

#### **Text S6: Importance of data likelihood in MLDA**

The design of the covariance matrix can prominently influence the Bayesian posterior  $\rho(\mathbf{m}|\mathbf{d}^{obs})$ . The results in Section 3.2 in the main text adopt  $\sigma_i^{SE} = 0.6$  m and  $\sigma_i^{NW} = 0.84$  m as uncertainties in fault-parallel offsets, accounting for both data noise and modeling errors due to the limited dimension of the model parameter  $n_m$ . Evaluating posteriorly, the offset misfits between the preferred models and the data are also comparable, with  $e^{SE} = 0.66$  m and  $e^{NW} = 0.99$  m. Therefore, although  $\sigma_i^{SE} = 0.6$  m and  $\sigma_i^{NW} = 0.84$  are still more than 10 times higher than the measurement accuracy (0.05 m) of fault-parallel offsets, these values still reasonably reflect the epistemic uncertainties due to the numerical models by assuming simple linear variations in plastic cohesion  $c$  and on-fault direct-effect parameter  $a$ . Additionally, we face further difficulties in training a stable surrogate model with the simple GPR model. Since the parameters  $\mathbf{m}$  in the models used for pretraining are generated randomly in the model space  $\mathcal{M}$ , it is difficult to generate effective samples



with high posterior probability densities. For example, reducing the standard deviations to  $\sigma_i^{SE} = 0.4$  m and  $\sigma_i^{NW} = 0.56$  m results in that only five out of the 87 models (red dots, Fig. 2 in the main text) have comparable probability densities; others are two orders of magnitude lower. Such few effective samples for pretraining lead to an unstable surrogate model at level  $l = 1$  in our MLDA algorithm.

We have also tested the influence of increasing the standard deviations in the covariance matrix of the likelihood function to  $\sigma_i^{SE} = 1.2$  m and  $\sigma_i^{NW} = 1.7$  m to check how it influences the inversion results (Fig. S5). The peaks in the 1D marginal distributions (diagonal panels) of the model parameters are  $\alpha_0 \approx 0.6$ ,  $\alpha_1 \approx 0.7$ , and  $\gamma_1 \approx 1.2$ , similar to the results with  $\sigma_i^{SE} = 0.6$  m and  $\sigma_i^{NW} = 0.84$  m. The only parameter with a different peak is the northwestern direct-effect scaling factor  $\alpha_0 \approx 1.1$  in Fig. S5k, whereas  $\alpha_0 \approx 0.8$  in Fig. 2k. The peak at  $\alpha_0 \approx 1.1$  comes from the group of models (within the red rectangles, Figs. S5c and f) that do not rupture the ground surface in the southeastern fault segment (Fig. S5k). This group of models is effectively rejected by setting lower uncertainties for fault-parallel offsets in the likelihood function, i.e.  $\sigma_i^{SE} = 0.6$  m and  $\sigma_i^{NW} = 0.84$  m. This sheds light on the importance of choosing adequate standard deviations in the likelihood function when epistemic uncertainties from the model assumptions are larger than the data noise. One effective method that we propose in this work is to choose standard deviations in the covariance matrix based on the misfits between the best-fit model and the data in a preliminary parameter space exploration, e.g. pre-training in our case, if the misfits are above the measurement accuracy of the data.

## Text S7: Convergence evaluation of the MLDA chains

The determination of burn-in length at the beginning of Markov chains is important in MCMC applications. MLDA inherits this property, and burn-in plays a significant role in designing the optimized parallelization strategy on supercomputing clusters with prefetching MLDA (Kruse et al., 2025). Each chain needs sufficient burn-in to ensure that the choice of the chains' starting point does not have a significant effect on the inversion results. Burn-in precludes scaling MCMC (and MLDA) by simply running large numbers of independent chains in parallel, since each individual chain brings in burn-in cost before contributing usable samples. For this reason, Kruse et al. (2025) show that the combination of pre-fetching and parallel chains can be an optimal choice in MLDA. In Section 2.4, we ignore the first 20 samples in each of the eight Markov chains as burn-in. After these 20 samples, the autocorrelation functions of the four model parameters drop below 0.1 and oscillate around zero (Fig. S6a), while the rank-normalized R statistics becomes smaller than 1.2 and further converge towards 1.0 (Fig. S6b). Both metrics indicate that the choice of 10 initial samples as burn-in is reasonable.

## Text S8: Real-time displacement at GNSS stations

We provide a comparison between the output of the models in the MLDA chains (blue curves) and the high-rate displacement recordings at 10 GNSS stations (Fig. 4) to show that the four-dimension model parameters  $\mathbf{m}$  are not sufficient to explain the dynamic surface displacement at some stations, such as CCCC, P580, and P595. The peaks in displacement of all models come earlier than those in the data. The time series achieve a better match at stations, such as P463, P570, and BEPK. These stations are located

in the north of the epicenter (Fig. 4). This indicates that dynamic rupture models may overestimate the rupture speed in the southeastern part of the fault F1.

### **Text S9: Inversion validation with data from seismic stations and moment release rate**

We compare the preferred models in our MLDA inversion with the reference model from Taufiqurrahman et al. (2023) at five seismic stations (blue rectangles, Fig. 4). Except for the station CCC, the velocity amplitudes and time histories are not prominently different from the reference model. This suggests that the velocities at the seismic stations are not sensitive to the model parameters  $\mathbf{m} = (\gamma_0, \gamma_1, \alpha_0, \alpha_1)$  in Table 1. They may be more sensitive to local velocity structures or other parameters in rupture dynamics.

The major difference in the moment release rate between the reference model and the preferred models is the amplitudes of the second moment rate peak (Fig. S10). However, the preferred models still maintain similar moment magnitudes ( $M_w \approx 6.98$ ) to the reference model ( $M_w \approx 7.01$ ). The moment magnitude is computed with

$$M_w = \frac{2}{3} \log_{10}(M_0) - 6.07, \quad (9)$$

where  $M_0$  is the seismic moment.

### **Text S10: Distribution of off-fault in-elastic deformation**

Off-fault inelastic deformation becomes larger and extends farther away from the fault at shallower depths (Fig. S11). We use a scalar plastic strain  $\eta$  to quantify the amplitude of inelastic off-fault deformation. Following Wollherr et al. (2018),  $\eta$  is defined as

$$\eta = \int_0^T \dot{\varepsilon}_{ij}^p \dot{\varepsilon}_{ij}^p dt, \quad (10)$$

where  $\dot{\varepsilon}_{ij}^p$  is the plastic strain rate (Wollherr et al., 2018) and  $T$  is the total simulation time.

## References

- Antoine, S. L., Klinger, Y., Delorme, A., Wang, K., Bürgmann, R., & Gold, R. D. (2021). Diffuse deformation and surface faulting distribution from submetric image correlation along the 2019 Ridgecrest, California, ruptures. *Bulletin of the Seismological Society of America*, 111(5), 2275–2302.
- Aochi, H., & Madariaga, R. (2003). The 1999 Izmit, Turkey, earthquake: Nonplanar fault structure, dynamic rupture process, and strong ground motion. *Bulletin of the Seismological Society of America*, 93(3), 1249–1266.
- Breuer, A., & Heinecke, A. (2022). Next-generation local time stepping for the ADER-DG finite element method. In *2022 IEEE International Parallel and Distributed Processing Symposium (IPDPS)* (pp. 402–413).
- Dunham, E. M., Belanger, D., Cong, L., & Kozdon, J. E. (2011). Earthquake ruptures with strongly rate-weakening friction and off-fault plasticity, part 1: Planar faults. *Bulletin of the Seismological Society of America*, 101(5), 2296–2307.
- Farr, T. G., Rosen, P. A., Caro, E., Crippen, R., Duren, R., Hensley, S., ... others (2007). The shuttle radar topography mission. *Reviews of geophysics*, 45(2).
- Goldberg, D. E., Melgar, D., Sahakian, V., Thomas, A., Xu, X., Crowell, B., & Geng, J. (2020). Complex rupture of an immature fault zone: A simultaneous kinematic model of the 2019 Ridgecrest, CA earthquakes. *Geophysical Research Letters*, 47(3), e2019GL086382.
- Good, I. J. (1963). Maximum entropy for hypothesis formulation, especially for multidi-

- 245 mensional contingency tables. *The Annals of Mathematical Statistics*, 34(3), 911–934.
- 246 Hauksson, E., Yoon, C., Yu, E., Andrews, J. R., Alvarez, M., Bhadha, R., & Thomas,  
247 V. (2020). Caltech/USGS Southern California Seismic Network (SCSN) and Southern  
248 California Earthquake Data Center (SCEDC): Data availability for the 2019 Ridgecrest  
249 sequence. *Seismological Research Letters*, 91(4), 1961–1970.
- 250 Kame, N., Rice, J. R., & Dmowska, R. (2003). Effects of prestress state and rupture  
251 velocity on dynamic fault branching. *Journal of Geophysical Research: Solid Earth*,  
252 108(B5).
- 253 Käser, M., Hermann, V., & Puente, J. d. l. (2008). Quantitative accuracy analysis of  
254 the discontinuous Galerkin method for seismic wave propagation. *Geophysical Journal  
255 International*, 173(3), 990–999.
- 256 Kristan, M., Leonardis, A., & Skočaj, D. (2011). Multivariate online kernel density  
257 estimation with Gaussian kernels. *Pattern recognition*, 44(10-11), 2630–2642.
- 258 Kruse, M., Niu, Z., Wolf, S., Lykkegaard, M., Bader, M., Gabriel, A.-A., & Seelinger, L.  
259 (2025). Scalable Bayesian inference of large simulations via asynchronous prefetching  
260 multilevel delayed acceptance. In *Proceedings of the platform for advanced scientific  
261 computing conference* (pp. 1–13).
- 262 Melgar, D., Melbourne, T. I., Crowell, B. W., Geng, J., Szeliga, W., Scrivner, C., ...  
263 Goldberg, D. E. (2020). Real-time high-rate GNSS displacements: Performance demon-  
264 stration during the 2019 Ridgecrest, California, earthquakes. *Seismological Research  
265 Letters*, 91(4), 1943–1951.
- 266 Noda, H., Dunham, E. M., & Rice, J. R. (2009). Earthquake ruptures with thermal  
267 weakening and the operation of major faults at low overall stress levels. *Journal of*



*Geophysical Research: Solid Earth*, 114(B7).

Schliwa, N., & Gabriel, A. (2023, 12). Equivalent near-field corner frequency analysis of 3d dynamic rupture simulations reveals dynamic source effects. *Seismological Research Letters*, 95(2A), 900-924. Retrieved from <https://doi.org/10.1785/0220230225> doi: 10.1785/0220230225

Schliwa, N., Gabriel, A.-A., & Ben-Zion, Y. (2025). Shallow fault zone structure affects rupture dynamics and ground motions of the 2019 Ridgecrest sequence to regional distances. *Journal of Geophysical Research: Solid Earth*, 130(6), e2025JB031194. doi: 10.1029/2025JB031194

Schliwa, N., Gabriel, A.-A., Premus, J., & Gallovič, F. (2024). The linked complexity of coseismic and postseismic faulting revealed by seismo-geodetic dynamic inversion of the 2004 Parkfield earthquake. *Journal of Geophysical Research: Solid Earth*, 129(12), e2024JB029410.

Taufiqurrahman, T., Gabriel, A.-A., Li, D., Ulrich, T., Li, B., Carena, S., ... Gallovič, F. (2023). Dynamics, interactions and delays of the 2019 ridgecrest rupture sequence. *Nature*, 618(7964), 308–315.

Terrell, G. R., & Scott, D. W. (1992). Variable kernel density estimation. *The Annals of Statistics*, 1236–1265.

Verdecchia, A., & Carena, S. (2016). Coulomb stress evolution in a diffuse plate boundary: 1400 years of earthquakes in eastern California and western Nevada, USA. *Tectonics*, 35(8), 1793-1811. doi: 10.1002/2015TC004091

Wang, H.-Y., Jiang, W.-P., Wang, S.-Y., & Miao, Y. (2019). In situ assessment of soil dynamic parameters for characterizing nonlinear seismic site response using kik-net

vertical array data. *Bulletin of Earthquake Engineering*, 17(5), 2331–2360.

Wollherr, S., Gabriel, A.-A., & Uphoff, C. (2018). Off-fault plasticity in three-dimensional dynamic rupture simulations using a modal Discontinuous Galerkin method on unstructured meshes: implementation, verification and application. *Geophysical Journal International*, 214(3), 1556–1584.

Yang, W., & Hauksson, E. (2013). The tectonic crustal stress field and style of faulting along the Pacific North America Plate boundary in Southern California. *Geophysical Journal International*, 194(1), 100–117.

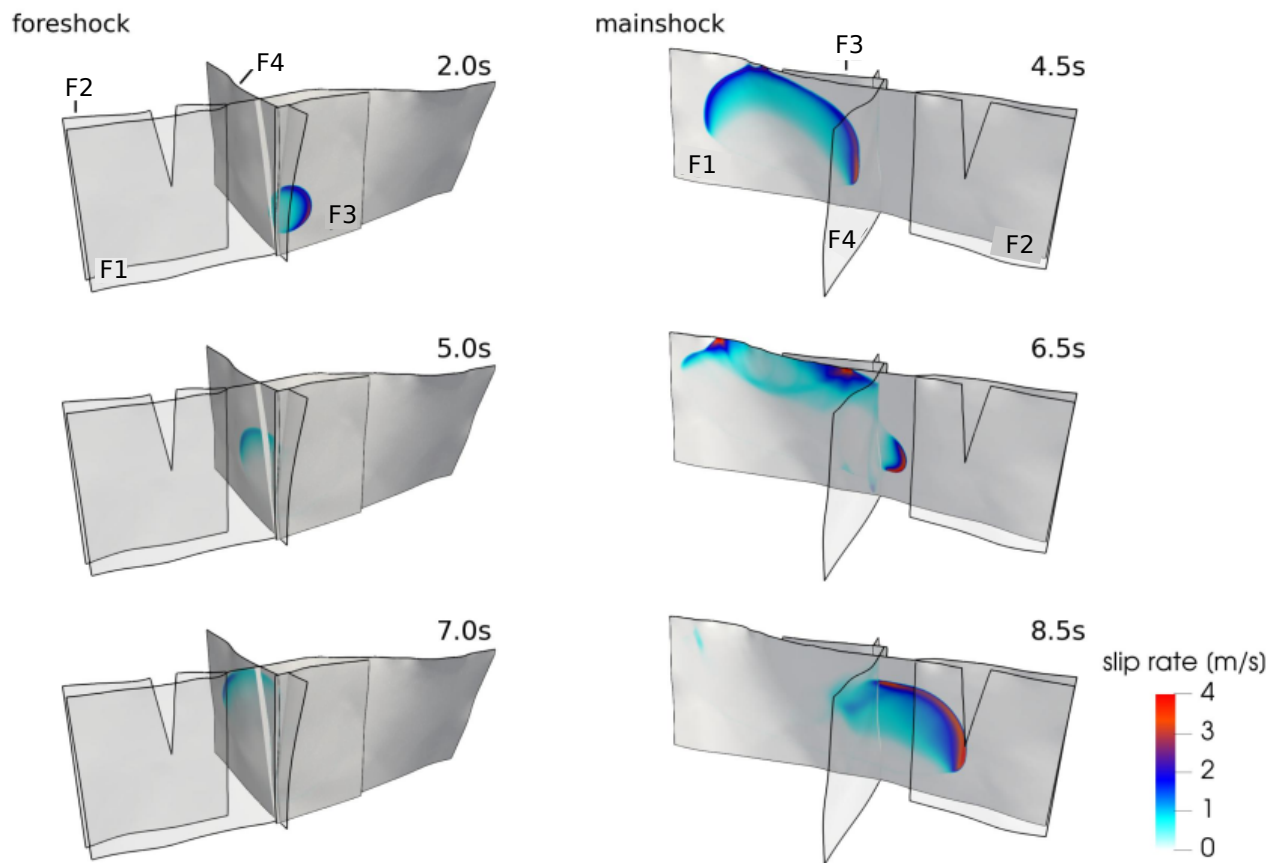


Figure S1: Snapshots of fault slip rate distribution during the Searles Valley foreshock and the Ridgecrest mainshock in the reference dynamic rupture model from Taufiqurrahman et al. (2023). The figure is adapted from Fig. S1 of Schliwa et al. (2025).

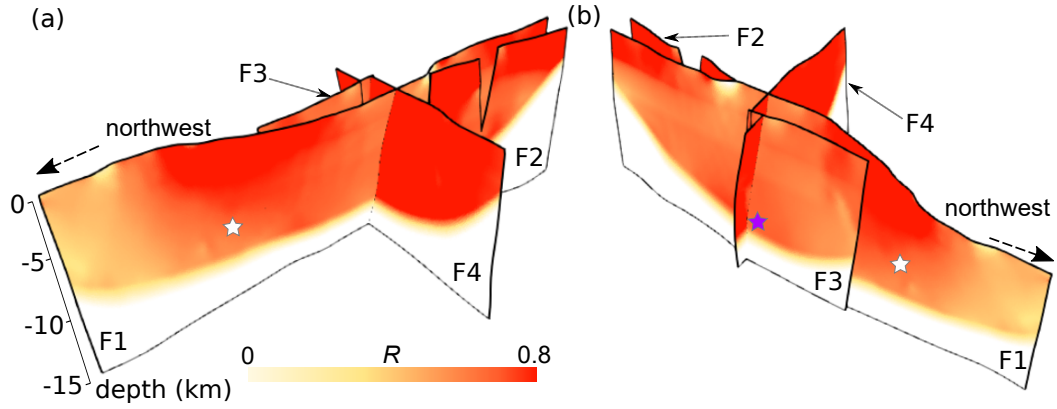


Figure S2: 3D fault structure that hosts the  $M_w$  7.1 mainshock (F1, F2, F4) and the  $M_w$  6.4 foreshock (F3, F4) from the reference model (Taufiqurrahman et al., 2023). The purple and white stars mark the hypocenters of the foreshock and the mainshock. The fault is color-coded with the prestress ratio  $R$  defined in Eq. (1).

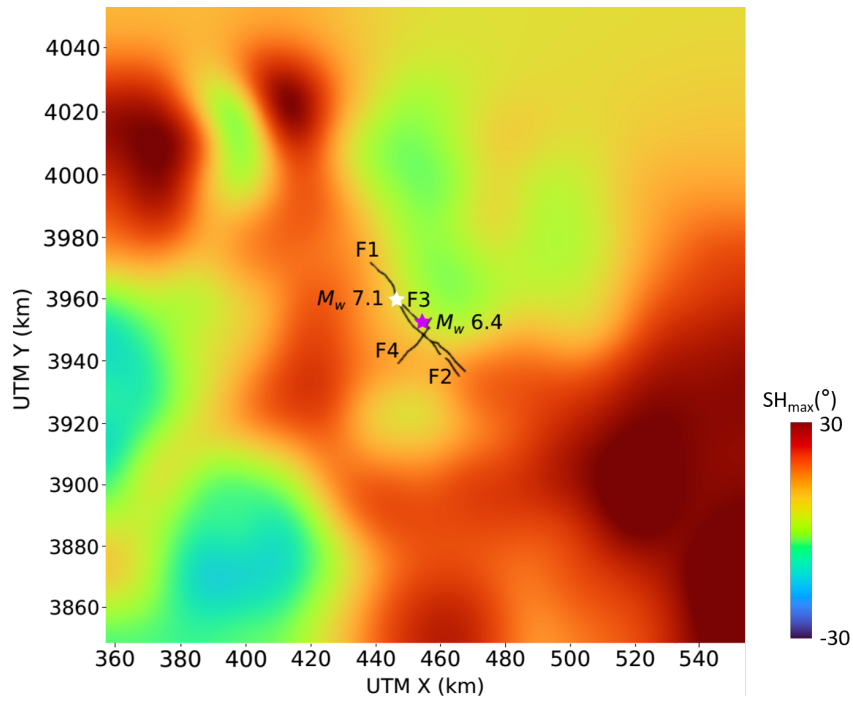


Figure S3: Map view of the 2D regional maximum horizontal stress orientation  $SH_{\max}$  from Yang & Hauksson (2013); Verdecchia & Carena (2016). The black curves mark the surface fault traces. The pink and white star are epicenters of, respectively, the foreshock and the mainshock.

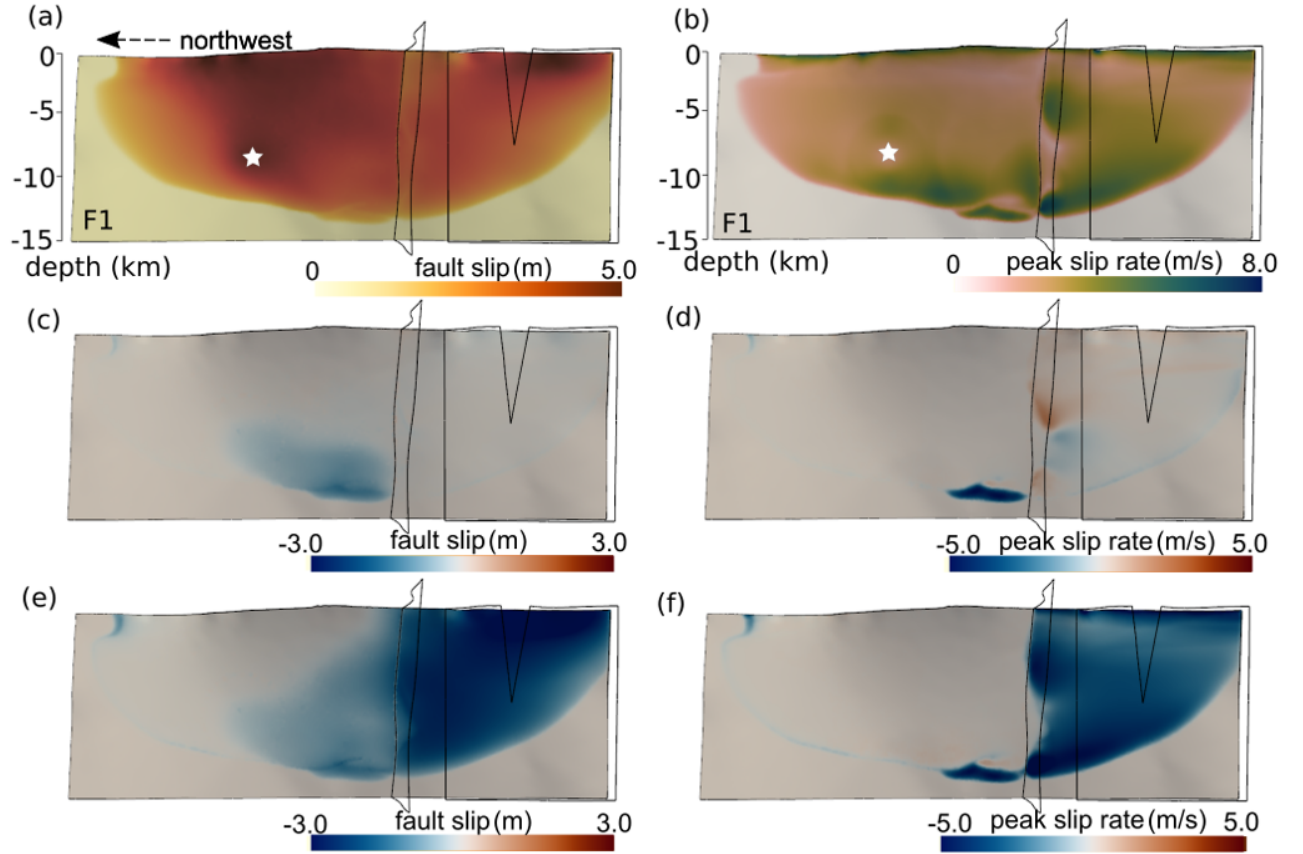


Figure S4: Fault slip (a) and peak slip rate (b) during the mainshock in the reference model (Taufiqurrahman et al., 2023). The white stars mark the hypocenter of the mainshock. Errors between our level-three model ( $l = 3$ ) and the reference model in the fault slip and the peak slip rate are in panel (c) and (d); while the errors of our level-two model ( $l = 2$ ) are in (e) and (f).



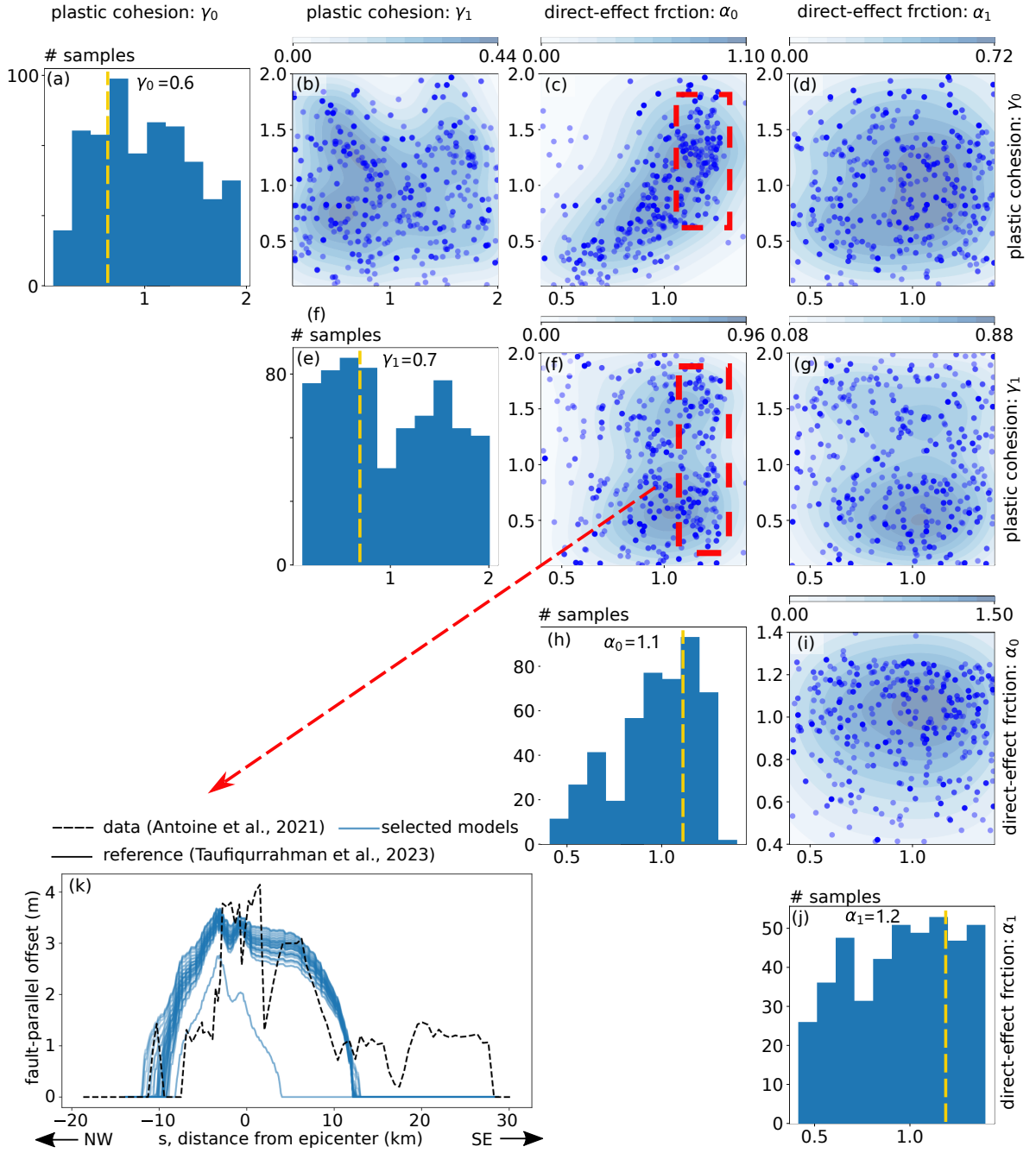


Figure S5: Panels of the Bayesian posterior  $\rho(\mathbf{m}|\mathbf{d}^{obs})$  from MLDA inversion. The diagonal panels from top to bottom are 1D marginal posterior probabilistic distribution of off-fault plastic cohesion ( $\gamma_0$ ,  $\gamma_1$ ) and on-fault direct-effect parameter in SVW-RS friction ( $\alpha_0$ ,  $\alpha_1$ ). The super-diagonal panels are the 2D marginal Bayesian posterior of each parameter pair from MLDA inversion. The blue dots are all the effective samples in the eight Markov chains. The density of the dots is color-coded in blue, which is proportional to the density  $\rho(\mathbf{m}|\mathbf{d}^{obs})$ . The density color-code is computed with the kernel density estimation with the Gaussian kernel (Terrell & Scott, 1992; Kristan et al., 2011). (k) Fault-parallel offset from model parameterizations within the red rectangles of panels (c) and (f). The fault-parallel offset data from Antoine et al. (2021) is shown in the dashed black curve.

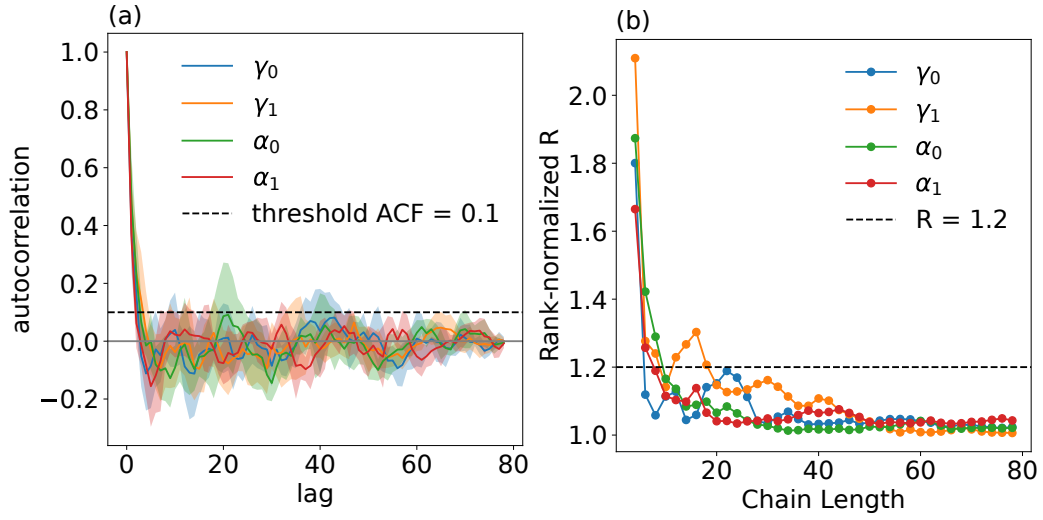


Figure S6: Analysis of the eight Markov chains in our MLDA algorithm. (a) Autocorrelation functions of the four model parameters  $\mathbf{m} = (\gamma_0, \gamma_1, \alpha_0, \alpha_1)$ . The solid curves are mean autocorrelation of the eight chains while the shading regions denote the standard deviation values of the eight chains. (b) Rank-normalized R statistics of the four model parameters  $\mathbf{m} = (\gamma_0, \gamma_1, \alpha_0, \alpha_1)$ .

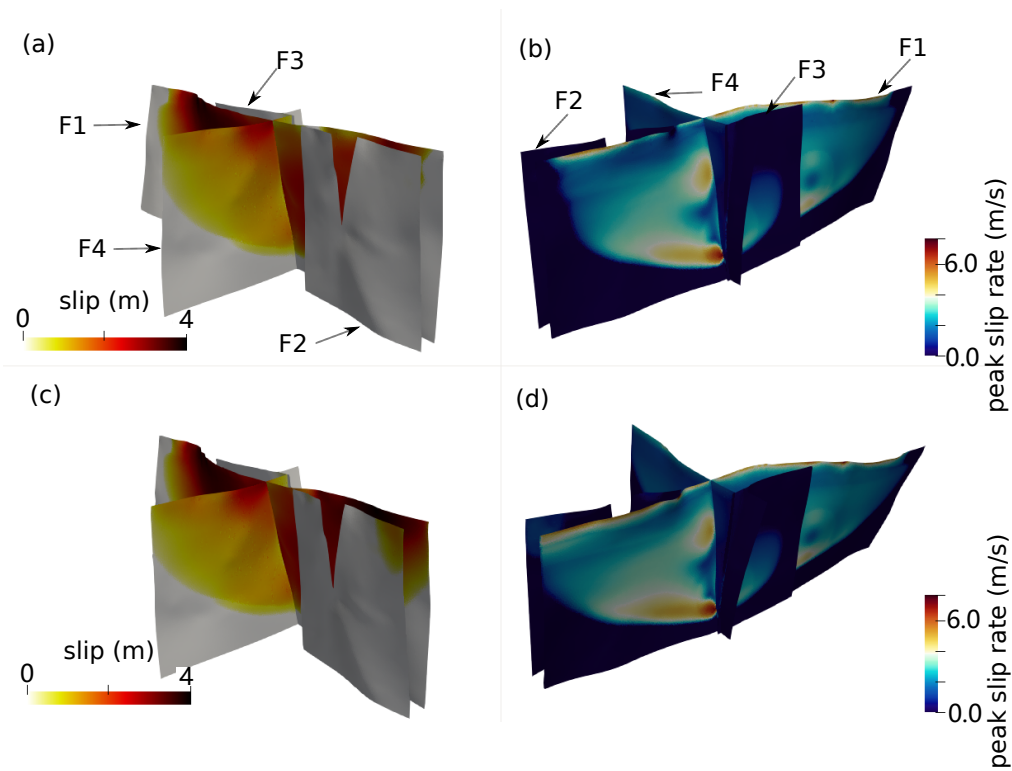


Figure S7: Comparison of the fault slip and peak slip rate during the mainshock between the preferred model (a,b) in the reference model (c,d). Panels a and c show, respectively, the fault slip of the preferred and the reference model; Panels b and d show, respectively, the peak slip rate of the preferred and the reference model.

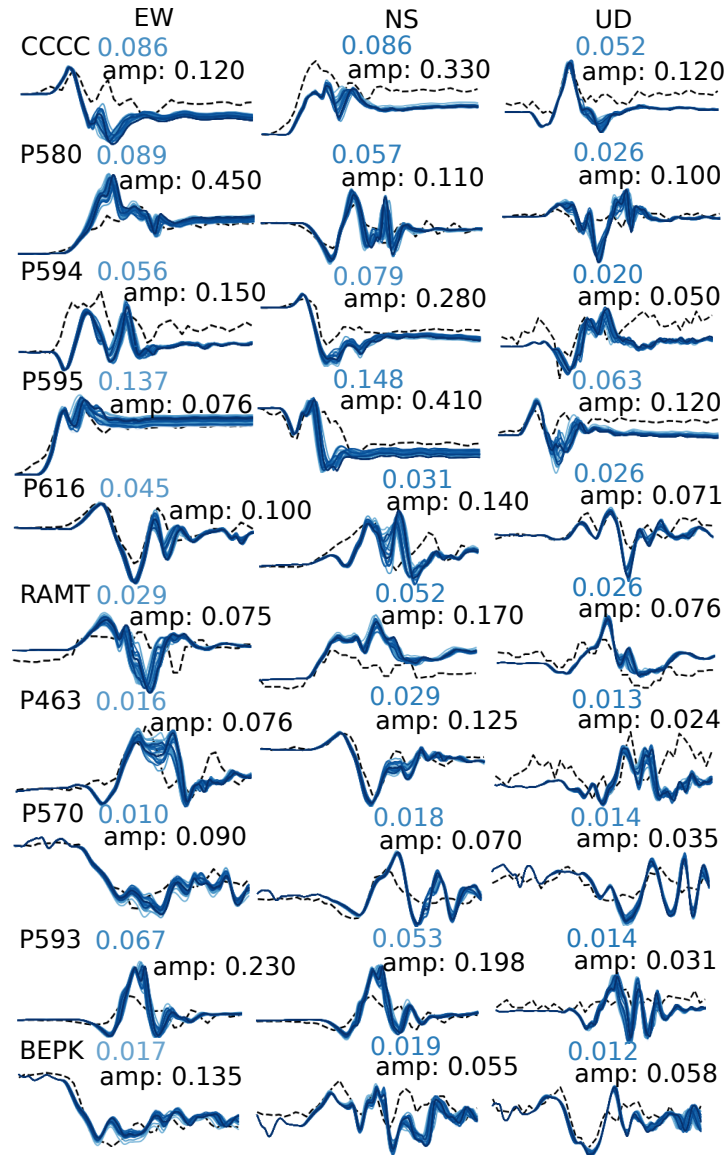


Figure S8: Supplementary results of Fig. 4. The three columns are 40 s of real-time displacement time series at the 10 high-rate GNSS stations in Fig. 4. From left to right, they show, respectively, east-west (EW), north-south (NS), and upward-downward (UD) components. The blue curves are simulation results from models in the MLDA chains. The black dashed curves are from the processed GNSS data by Melgar et al. (2020). The black numbers mark the peak amplitudes in meters of the time series in each sub-panel. The blue numbers are L2 misfits in meters between the simulation outputs and the data.

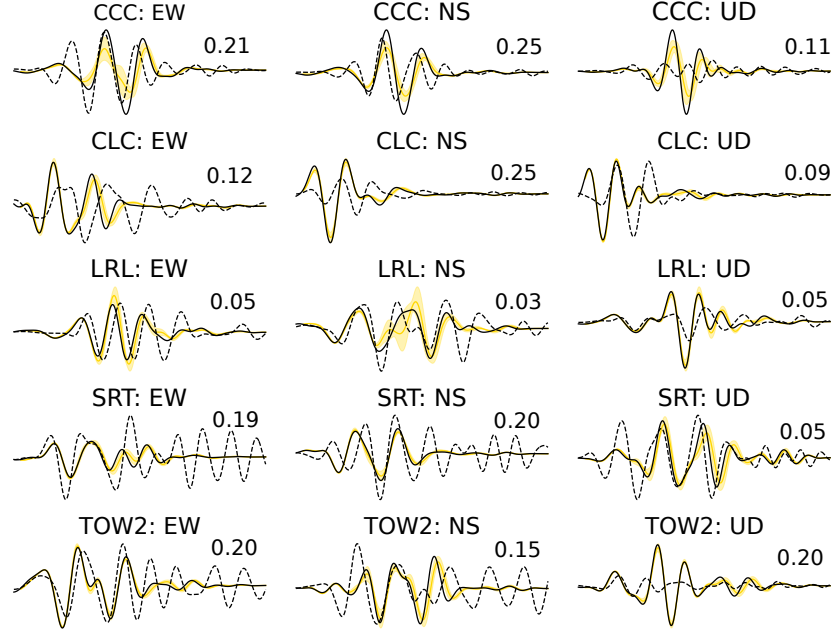


Figure S9: 40 s of velocity time series at the 5 seismic stations in Fig. 1 in the main text, bandpass filtered between 0.1 and 0.3 Hz. From left to right, they show, respectively, east-west (EW), north-south (NS), and upward-downward (UD) components. The dashed black curves are data from Hauksson et al. (2020); the solid curves are from the reference model of Taufiqurrahman et al. (2023); and the yellow curves are the mean of the preferred models with one standard deviation in yellow shading. The numbers in each panels are the amplitudes of the waveform in m/s. The waveforms in the same panel are scaled by the same factor.

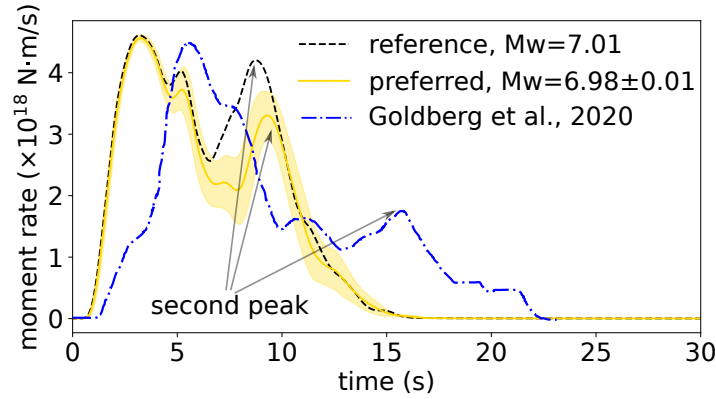


Figure S10: Comparison of the time history of the moment release rate between the preferred models (Fig. 2 in the main text) and the reference model by Taufiqurrahman et al. (2023). The solid curve is from the reference model by Taufiqurrahman et al. (2023); the yellow curve is the mean of the preferred models with one standard deviation in yellow shading; and the blue dashed-dotted curve is from the kinematic source inversion by Goldberg et al. (2020).



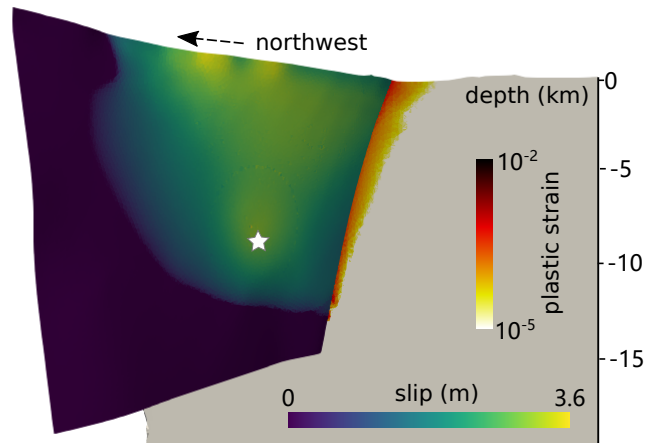


Figure S11: Distribution of off-fault plastic strain  $\eta$  in the off-fault rocks and the fault slip around the intersection A-A' in Fig. 5b. The white star marks the earthquake hypocenter.

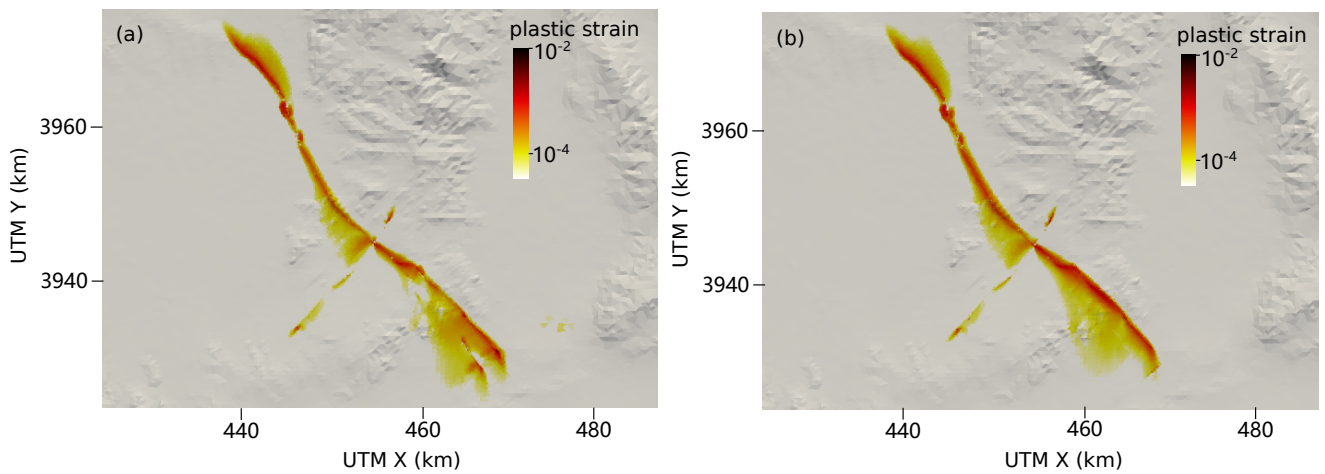


Figure S12: Map view of plastic strain  $\eta$  in the off-fault rocks from the reference model (a) and the preferred model (b).

Table S1: Differences in outputs at GNSS stations and fault-parallel offsets (FO) from models at level three and level two of our prefetching MLDA algorithm, compared with the high-resolution model (Taufiqurrahman et al., 2023). The differences are compared with the standard deviations (std inv.) of the likelihood function in Eq. (8) in the main text. The three rows that correspond to each GNSS station are EW (east-west), NS (north-south), and UD (upward-downward) components from top to bottom. In the inversion, we do not use the UD component of the 11 GNSS stations with static displacement data, and fill the corresponding fields with “-”. The last two rows in the forth column of the table correspond to offsets at  $s < 10$  km and  $s > 10$  km in the fault-parallel coordinate (Fig. 1a). The values are in millimeter.

high-rate	level 3	level 2	std inv.	static	level 3	level 2	std inv.
CCCC	7.0	103.9	64.0	DTPG	1.2	4.0	10.0
	8.3	30.6	59.0		2.4	37.9	10.0
	3.4	13.7	52.0		0.3	17.5	-
P580	16.0	146.7	110.0	P569	3.7	59.8	10.0
	14.1	27.5	40.0		1.8	1.2	10.0
	9.8	25.3	40.0		3.7	1.9	-
P594	5.7	26.4	40.0	CPBN	1.9	9.1	10.0
	10.5	96.7	40.0		3.0	43.3	10.0
	2.3	9.6	40.0		3.6	11.7	-
P595	28.3	203.0	40.0	P590	0.6	19.3	10.0
	18.5	235.3	110.0		5.1	44.5	10.0
	16.2	29.4	40.0		1.3	22.9	-
P616	3.1	27.6	64.0	P592	0.7	2.6	10.0
	4.8	34.3	120.0		4.0	52.1	10.0
	2.2	8.0	40.0		0.1	19.3	-
RAMT	3.5	28.2	57.0	GOLD	4.6	45.3	10.0
	5.4	33.3	40.0		3.5	2.4	10.0
	1.9	7.9	40.0		1.1	39.7	-
P463	3.3	20.5	40.0	WORG	1.6	63.4	10.0
	3.7	24.6	40.0		2.1	9.0	10.0
	1.3	4.8	40.0		4.0	3.4	-
P570	3.6	21.1	40.0	COSO	3.4	104.2	10.0
	1.4	5.0	40.0		1.8	94.4	10.0
	1.5	8.4	80.0		0.5	9.7	-
P593	11.0	43.9	40.0	P464	0.3	4.5	10.0
	7.7	34.3	40.0		5.8	82.4	10.0
	2.9	7.1	40.0		0.3	19.6	-
BEPK	4.0	20.1	40.0	P596	1.2	26.9	10.0
	4.3	14.6	40.0		0.6	4.2	10.0
	2.2	7.7	40.0		0.9	10.1	-
FO	32.2	523.2	840.0	P597	0.1	81.7	10.0
	24.0	1323.1	600.0		0.5	0.0	10.0
	-	-	-		3.2	10.7	-